AGU PUBLICATIONS

JGR

Journal of Geophysical Research: Space Physics

RESEARCH ARTICLE

10.1002/2016JA022689

The response of clouds and aerosols to cosmic ray decreases

J. Svensmark[1], M. B. Enghoff[1], N. J. Shaviv[2], and H. Svensmark[1]

[1]National Space Institute, Technical University of Denmark, Lyngby, Denmark, [2]Racah Institute of Physics, Hebrew University of Jerusalem, Jerusalem, Israel

Key Points:
- Ranking of Forbush decreases after their strength
- Formulation of a Monte Carlo statistical model to test the significance of the impact Forbush decreases on clouds
- A significant response is found in all studied aerosol and cloud data suggesting that cosmic ray ionization is important for cloud physics

Correspondence to:
H. Svensmark,
hsv@space.dtu.dk

Citation:
Svensmark, J., M. B. Enghoff, N. Shaviv, and H. Svensmark (2016), The response of clouds and aerosols to cosmic ray decreases, *J. Geophys. Res. Space Physics*, *121*, 8152–8181, doi:10.1002/2016JA022689.

Received 9 MAR 2016
Accepted 14 AUG 2016
Accepted article online 19 AUG 2016
Published online 1 SEP 2016

Abstract A method is developed to rank Forbush decreases (FDs) in the galactic cosmic ray radiation according to their expected impact on the ionization of the lower atmosphere. Then a Monte Carlo bootstrap-based statistical test is formulated to estimate the significance of the apparent response in physical and microphysical cloud parameters to FDs. The test is subsequently applied to one ground-based and three satellite-based data sets. Responses (>95%) to FDs are found in the following parameters of the analyzed data sets. AERONET: Ångström exponent (cloud condensation nuclei changes), SSM/I: liquid water content, International Satellite Cloud Climate Project (ISCCP): total, high, and middle, IR-detected clouds over the oceans, Moderate Resolution Imaging Spectroradiometer (MODIS): cloud effective emissivity, cloud optical thickness, liquid water, cloud fraction, liquid water path, and liquid cloud effective radius. Moreover, the responses in MODIS are found to correlate positively with the strength of the FDs, and the signs and magnitudes of the responses agree with model-based expectations. The effect is mainly seen in liquid clouds. An impact through changes in UV-driven photo chemistry is shown to be negligible and an impact via UV absorption in the stratosphere is found to have no effect on clouds. The total solar irradiance has a relative decrease in connection with FDs of the order of 10^{-3}, which is too small to have a thermodynamic impact on timescales of a few days. The results demonstrate that there is a real influence of FDs on clouds probably through ions.

1. Introduction

Galactic cosmic rays (GCRs) are thought to affect cloud cover on Earth, through ionization and subsequent effects on aerosol processes [*Dickinson*, 1975; *Svensmark and Friis-Christensen*, 1997; *Marsh and Svensmark*, 2000; *Bagó and Butler*, 2000]. A prevalent approach to evaluating this idea has been to investigate effects of coronal mass ejections—events where a cloud of magnetized plasma is ejected from the solar corona and travels out into interplanetary space. This ejected plasma cloud tends to screen out galactic cosmic rays from its interior and if the plasma cloud hits Earth, it may result in a sudden decrease in the amount of cosmic rays reaching the atmosphere as measured by neutron monitors. Such an event, known as a Forbush decrease (FD) [*Forbush*, 1937], may evolve within hours, with the depression in cosmic ray counts recovering over a week or more, as the plasma cloud passes Earth and continues farther out from the Sun. An example of a FD is shown in Figure 1. Fewer cosmic rays generate less ionization in the atmosphere, such that these events present an opportunity for testing the cosmic ray/cloud link.

Svensmark et al. [2009] found a significant signal in both aerosols (specifically the aerosol Ångström exponent) and liquid, low clouds. However, a debate is still ongoing with regard to whether there actually is an effect. Studies by *Sloan and Wolfendale* [2008], *Laken et al.* [2009], *Calogovic et al.* [2010], and *Laken and Calogovic* [2011] found no statistically significant signal during or following FDs. *Kristjánsson et al.* [2008] and *Todd and Kniveton* [2004] found some response in cloud satellite data, while *Pudovkin and Veretenenko* [1995], *Harrison and Stephenson* [2006], and *Harrison and Ambaum* [2010] found a response based on surface observations. A signal in middle- and high-level clouds has been reported by *Rohs et al.* [2010], and *Dragić et al.* [2011] found a signal by using the diurnal temperature range as a cloud proxy, which allowed them to extend the data range farther back than the onset of satellite measurements.

Experimentally, it has been shown that ions do promote the formation of new small (3 nm sized) aerosols [*Svensmark et al.*, 2007; *Kirkby et al.*, 2011], and one experiment suggests that ions also help the growth of aerosols to cloud condensation nuclei sizes (>50 nm) [*Svensmark et al.*, 2013]. However, from a modeling point of view, it is uncertain whether a variation in ion-induced nucleation may translate into an observable change

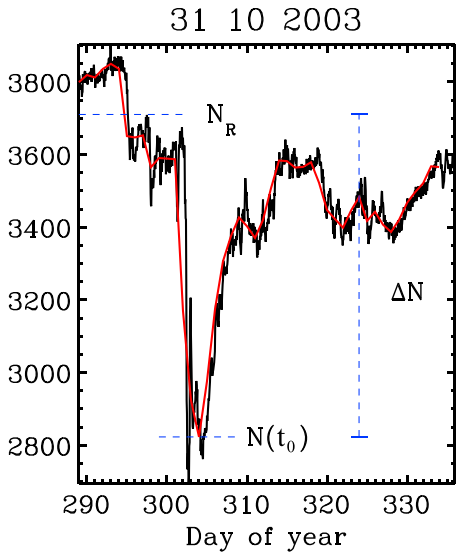

Figure 1. The large Forbush decrease of 2003 with the minimum in the daily averaged signal occurring on 31 October as recorded by the CLIMAX neutron monitor. The black and red lines, respectively, correspond to the hourly and daily averaged values. The latter is used in this work. N_R is the reference level before the FD, while $N_{min} = N(t_0)$ is the daily averaged minimum value during the FD (see text).

in cloud condensation nuclei (CCN) and thus in clouds. *Bondo et al.* [2010] suggest that an aerosol effect could be observable under atmospheric conditions while general circulation modeling gives rise to much smaller responses in the CCNs [*Kazil et al.*, 2006; *Pierce and Adams*, 2009; *Snow-Kropla et al.*, 2011; *Yu and Luo*, 2014]. Of these studies, *Yu and Luo* [2014] find a response almost an order of magnitude larger than previous estimates but still insufficient to explain the large observed variations in the ocean heat content over the solar cycle [*Shaviv*, 2008; *Howard et al.*, 2015]. The above uncertainties make it is desirable to use observations to better constrain a possible effect.

The present work aims to improve on previous statistical strategies, as well as apply these to both previously examined and unexamined cloud and aerosol data. We consider in depth the behavior of several cloud parameters during FDs and compare with cloud theory. We also improve on the treatment of potential effects from total solar irradiance (TSI) and ultra violet (UV) light during FDs by taking a solar spectral approach, rather than a UV tracer approach as done in previous studies.

Four independent atmospheric data sets are used and described in section 2. They include a land-based set of measurements of aerosol optical thickness probing the amount of small aerosols and three distinct satellite-based cloud data sets measuring a range of physical and microphysical cloud parameters. Data from one or more of the above four independent sources have all been used in previous studies [*Todd and Kniveton*, 2004; *Kristjánsson et al.*, 2008; *Sloan and Wolfendale*, 2008; *Svensmark et al.*, 2009; *Laken et al.*, 2009; *Calogovic et al.*, 2010].

The response in atmospheric parameters is expected to depend on the strength of the FDs, namely, if a given FD produces a larger change in atmospheric ionization, it should correspondingly induce a relatively large response in the atmospheric variables. A method to estimate the strength of individual FDs was used implicitly in *Svensmark et al.* [2009]. In order to make the present paper self-contained, the full method is presented in section 3.

The statistical model is defined in section 4. This model is based on Monte Carlo bootstrap statistics, and it takes the finite growth time of aerosols into account. This statistical model is applied to each of the four data sets in section 5, and the resulting statistical significance is then determined. The rich Moderate Resolution Imaging Spectroradiometer (MODIS) data allow for the study of six relevant cloud parameters. If there exists a link between cosmic rays, aerosols, and clouds, a change in several cloud parameters can reasonably be expected on a global scale during a FD, where the sign and magnitude of the response should concur with expected cloud microphysics. In section 6, the expected parameter changes are calculated and compared to the results of the MODIS data set.

Last, the results are discussed in section 7 and placed in context of possible mechanisms involving changes in the GCR flux, the Total Solar Irradiance (TSI), or UV light.

2. Data

A number of data sets related to cosmic rays, total solar irradiance, ultraviolet radiation, atmospheric aerosols, and global cloud cover serving as the basis for the present analysis are presented below.

2.1. Neutron Monitor and Muon Data

Cosmic ray variations at Earth have been monitored by either neutron monitors or by muon detectors. Both neutrons and muons are among the secondary particles produced when primary cosmic ray particles interact with atomic nuclei in the atmosphere, and the aforementioned detectors may therefore be used for probing the primary cosmic ray spectrum.

In this study we employ neutron monitor data from all available stations within the temporal range 1987–2014. The number of stations amounts to about 130 with cutoff rigidity in the range 0–47 GV. Neutron monitor data can be obtained from the World Data Center for Cosmic Rays (WDCCR, http://center.stelab.nagoya-u.ac.jp/WDCCR/). Muon data are from the Multi-Directional Cosmic Ray Muon Telescope at Nagoya and covers a cutoff rigidity of 60–119 GV. (http://www.stelab.nagoya-u.ac.jp/ste-www1/div3/muon/muon1.html).

2.2. Solar Spectrum Data

For the analysis of the temporal variations in the solar electromagnetic spectrum we employ data from either composite solar spectral irradiance in the wavelength range 120–400 nm covering the time period 8 November 1978 to 1 August 2005 [*DeLand and Cebula*, 2008] or the Solar Radiation and Climate Experiment (SORCE) in the wavelength range 115–2416 nm covering the temporal period 14 April 2003 to 24 August 2015 (http://lasp.colorado.edu/home/sorce/data/). Furthermore, we use total solar irradiance (TSI) data from the VIRGO Experiment on the cooperative ESA/NASA Mission SOHO (version d41_61_0803) from PMOD/WRC.

2.3. Atmospheric Data

The atmospheric data used in this study are

1. observational data on aerosols in the atmosphere obtained from the solar photometers of the aerosol robotic network (AERONET) program [*Schuster et al.*, 2006]. This data set is based on surface observations from more than 700 stations.
2. observations of cloud liquid water content (CWC) over the world's oceans observed by the Special Sounder Microwave Imager (SSM/I) [*Wentz*, 1997; *Weng et al.*, 1997]. The SSM/I instrument is flown on board the DMSP satellites and measures radiance in the microwave range. The daily data cover the period of July 1987–present.
3. IR-detected measurements of high, mid, low, and total IR clouds from the International Satellite Cloud Climate Project (ISCCP) [*Rossow and Schiffer*, 1991], using a temporal resolution of 3 h (the D1 data).
4. daily observations of six key cloud parameters measured by the Moderate Resolution Imaging Spectroradiometer (MODIS) [*Salomonson et al.*, 1989] aboard the Terra satellite. The parameters are (1) the cloud effective emissivity (ϵ), (2) the cloud optical thickness (τ), (3) the liquid water cloud fraction (CF, previously examined in *Svensmark et al.* [2009]), (4) the column density of CCNs, (5) the liquid water path (LWP), and (6) the liquid cloud effective radius (R_{eff}), all from the "MOD08_D3" product. The ice cloud fraction is also used to a smaller degree.

3. Variations in the Primary Cosmic Ray Spectrum Caused by Forbush Decreases

Measurements of the temporal evolution of the cosmic ray flux are primarily made by neutron monitors and to a lesser extent by muon telescopes. Since the response of neutron monitors depends on the location (latitude, longitude, and altitude) of the monitor, the monitors are sensitive to different parts of the primary cosmic ray energy spectrum. This fact will be used in the following to extract information on the variation in the primary cosmic ray energy spectrum during a FD. The primary spectral changes are important since they can be used to determine the changes in ionization throughout Earth's atmosphere, and thus be used to rank the strength of the FDs according to impact on ionization.

3.1. Extraction of the Primary Cosmic Ray Spectrum

Individual FDs are identified over a period of almost three decades together with responses in the global network of about 130 neutron monitors (NMs) and muons from the Multi-Directional Cosmic Ray Muon Telescope at Nagoya. The change in the primary cosmic ray spectrum at Earth (at 1 AU) during a FD cannot be known from a single neutron monitor, as the response is related to an integral over the cosmic ray spectrum and the response function of the neutron monitor. It is, however, possible to extract variations in the cosmic ray spectrum using multiple cosmic ray detectors as will be shown in the following.

A neutron monitor counts mainly the neutrons that are produced in the secondary shower events following the nuclear interactions of a primary cosmic ray particle with an atom high in Earth's atmosphere. Count rates, $N(t)$, that a NM registers depend on the altitude and geomagnetic position of the instrument and is given by

$$N(t) = \int_{P_c}^{\infty} S(h,P)J(P,t)\mathrm{d}P, \tag{1}$$

where P is the rigidity defined as $P = pc/q$, p and q, respectively, are the momentum and charge of the primary cosmic ray particle, and c is the speed of light. P_c is the cutoff rigidity due to the geomagnetic field and $S(h,P)$ is the yield or response function (the average number of counts in the NM, located at a height h above sea level, due to a primary cosmic ray particle of rigidity P) [*Clem and Dorman*, 2000]. $J(P,t)$ is the differential rigidity spectrum at 1 AU as a function of time t. Here $J(P,t)$ is the unknown function whose variation during a FD we are aiming at estimating.

From the above equation, one can define the median rigidity P_m as

$$\frac{N(t)}{2} = \int_{P_c}^{P_m} S(h,P)J(P,t)\mathrm{d}P, \tag{2}$$

i.e., the rigidity below which the NM registers 50% of its counts. The median rigidity characterizes a NM, since it depends on the location. One feature of the median rigidity is that it changes through the solar cycle. This is not a serious problem in the present study, since FDs are most frequent around solar maximum. We, therefore, elect to use the median rigidity at solar maximum for all NMs. The median rigidity of the NM data is based on vertical cutoff rigidity estimates and ranges from ≈10 GV (South Pole stations) to ≈47 GV (Ahmedabad, India). The multidirectional muon detector at Nagoya has 17 different viewing angles and represents 17 different paths of the muons through the atmosphere and, therefore, 17 different response functions. The median rigidity range of the Muon Telescope ranges from 60 GV to 119 GV. Together, the NMs and muon detector used in the present work cover the range from 10 GV to 119 GV in median rigidity. The analysis is based on daily averages.

Forbush decreases are here identified in the South Pole neutron monitor data as events having a relative decrease of at least 7%. This neutron monitor is used since it has the smallest cutoff rigidity of all monitors and thus has the largest response. When a FD is identified, the day t_0 over which the minimum number of counts $N(t_0)$ occurs is found. Then, data from all operational neutron monitors at that particular date are used to obtain reference levels, N_R, prior to the minimum of the FD, defined as

$$N_R \equiv \frac{1}{15}\sum_{t=t_0-15}^{t_0-1} N(t), \tag{3}$$

i.e., a 15 day average of the neutron counts ending 1 day prior to the minimum. From this, the change in neutron counts is defined as

$$\Delta N \equiv N(t_0) - N_R, \tag{4}$$

and the relative change is defined as

$$\delta N \equiv \frac{\Delta N}{N_R}. \tag{5}$$

N_R, ΔN, and $N(t_0)$ are illustrated in Figure 1 for the strong FD event of 31 August 2003, as registered by the CLIMAX NM. It is possible to extract $\delta N_{j,k}$ for each of the operational NMs, where the index j identifies the NM, and index k the particular FD event.

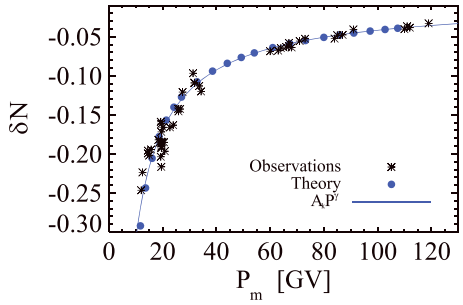

Figure 2. Relative changes of counts by neutron monitors and the Nagoya Muon Telescope plotted against the median rigidity P_m of the stations, for the strong FD of 31 August 2003 (black star symbols). The blue curve shows the least squares fitted empirical function of equation (6), with the parameters $A = 229$ and $\gamma = -0.87$. The blue line can also represent an exact theoretical relative change in the primary spectrum $\delta J_k/J_0 = A_k P^{-\gamma k}$ as indicated by equation (8). Blue symbols are the relative changes in cosmic ray counts as a function of the median cutoff rigidity P_m, calculated for a standard NM-64 neutron monitor response function and are a test of the approximation given by equation (13). The good agreement between the points and the curve demonstrates that the approximation is adequate and thus suggests that changes in the primary cosmic ray spectrum during FDs can be derived and quantified using the proposed method (see text).

Figure 2 depicts the extracted relative change δN in the primary spectrum for a sample FD event. The data points correspond to measurements by neutron monitors operational at the particular date as function of median rigidity, evaluated at solar maximum. The group of points above 60 GV are from the Multi-Directional Cosmic Ray Muon Telescope at Nagoya. One can then fit the data points with the functional form

$$\delta n_k = -A_k P^{\gamma_k}, \tag{6}$$

where the amplitude A_k and the exponent γ_k are determined by a least squares fit, while the index k refers to the specific FD being investigated, and P is measured in gigavolts. The functional form of δn_k given in equation (6) is regularly used as a good approximation to FD modulations of the energy spectra [*Ahluwalia and Fikani*, 2007]. The blue line in Figure 2 is the result of a least squares fit of the above functional form to the strong FD event of 31 October 2003, resulting in the parameters $A = 229$ and $\gamma = -0.87$.

Using equation (6), the relation between the primary unperturbed differential rigidity spectrum $J_0(P, t)$ and the perturbed spectrum J_k

$$J_k = \left(1 - A_k P^{\gamma_k}\right) J_0(P, t), \tag{7}$$

such that the change in the primary differential rigidity spectrum is

$$\delta J_k = J_k(P, t) - J_0(P, t) = -A_k P^{\gamma_k} J_0(P, t). \tag{8}$$

It is now possible to relate between the responses in neutron monitors and the primary spectrum. The reference level derived from the detector counts is given by

$$N_R = \frac{1}{15} \int_{P_c}^{\infty} \int_{t_0-15}^{t_0-1} S(h, P) J_0(P, t)\, \mathrm{d}t\, \mathrm{d}P, \tag{9}$$

$$= \int_{P_c}^{\infty} S(h, P) J_R(P)\, \mathrm{d}P, \tag{10}$$

where

$$J_R(P) = \frac{1}{15} \int_{t_0-15}^{t_0-1} J_0(P, t)\, \mathrm{d}t, \tag{11}$$

and the minimum count during a FD is given by,

$$N(t_0) = \int_{P_c}^{\infty} S(h, P) \left(1 - A_k P^{\gamma_k}\right) J_0(P, t_0)\, \mathrm{d}P. \tag{12}$$

By letting $J_R(P) = J_0(P, t_0)$ the relative change δN (see equation (5)) becomes

$$\begin{aligned}\delta N &= -\frac{\int_{P_c}^{\infty} S(h,P)(A_k P^{\gamma_k}) J_R(P)\mathrm{d}P}{\int_{P_c}^{\infty} S(h,P) J_R(P)\mathrm{d}P} \\ &= -\frac{2\int_{P_c}^{P_m} S(h,P)(A_k P^{\gamma_k}) J_R(P)\mathrm{d}P}{2\int_{P_c}^{P_m} S(h,P) J_R(P)\mathrm{d}P} \\ &= -A_k {P_0}^{\gamma_k} \frac{\int_{P_c}^{P_m} S(h,P) J_R(P)\mathrm{d}P}{\int_{P_c}^{P_m} S(h,P) J_R(P)\mathrm{d}P} \\ &= -A_k {P_0}^{\gamma_k} \approx -A_k {P_m}^{\gamma_k}.\end{aligned} \tag{13}$$

To derive the second line of equation (13), the integration limits are changed using equation (2), while it is noted in the third line that $S(h,P)J_R(P)$ does not change sign and that the mean value theorem for integrals can be used to take $-A_k {P_0}^{\gamma_k}$ out of the integration, where P_0 is in the interval $P_c \le P_0 \le P_m$. Finally P_0 is approximated by P_m.

Using the final form of equation (13) it is then possible to extract any spectral changes between two different sets of observations on any timescale relevant for GCR monitors. In particular, one can compare observations between solar maximum and solar minimum during solar cycles number 21–23, and characterize the spectral changes over the solar cycle with $A_{SC} = 336 \pm 46$ and $\gamma_{SC} = -1.10 \pm 0.04$ [*Svensmark et al.*, 2009]. This measure can then be used to relate the spectral changes during each FD to the spectral changes over a solar cycle.

We continue by testing the above approximations numerically. With the aid of a response function $S(P,h)$ for an NM-64 neutron monitor [*Clem and Dorman*, 2000; *Flückiger et al.*, 2008], one can calculate the relative change in the monitor counts δN for a given A_k and γ_k, as a function of the monitor's cutoff rigidity, P_c, using equations (10) and (12). The relative change, δN calculated from the neutron monitor's response, can then be compared with the relative change in the differential rigidity spectrum, $\delta J_k/J_0 = A_k {P_m}^{-\gamma}$, (equation (8)). The solid line in Figure 2 denotes $A_k P^{-\gamma}$, while the blue dots correspond to the numerically determined relative decrease δN, as a function of the numerically determined P_m, (using equation (2)). Figure 2 demonstrates that the approximation is satisfactory to within a few percent. The largest errors are for the lower median rigidities. Although the above test was not performed for a muon detector response function, there is no reason to suspect that our approximations are less valid in that case, as the response functions are of a similar form.

With a threshold of 7% in the South Pole neutron monitor, a total of 26 events are found between 1989 and 2005. For each event, all available neutron monitors together with the Nagoya muon telescope are used to estimate the relative maximal decrease during the FD as a function of the monitors stated median rigidity P_m. With the methods outlined above, it is then possible to extract the change in the primary cosmic ray spectrum for each FD. Table 1 summarizes the 26 largest FD events identified in this way. We proceed in the next section to rank the events according to their change in atmospheric ionization.

3.2. Variation in the Atmospheric Ionization

The (maximal) change in the differential rigidity spectrum during a FD can be extracted by applying the methods outlined in the previous section. With it, one can calculate the resulting change in the ion production throughout the atmosphere. This is carried out through a Monte Carlo simulation of primary CRs incoming at different energies and the resulting shower structure of secondary particles. Specifically, the evolution of the shower is calculated using the CORSIKA code [*Heck et al.*, 1998], where a primary cosmic ray proton of kinetic energy T and an incident angle from the zenith in the interval $0 \le \alpha \le 70°$ are the initial conditions for the cascade. Note that *Usoskin and Kovaltsov* [2006] have developed a model of atmospheric ionization based on similar methods where they use zenith angles up to 90°. For any primary particle energy, 10,000 showers are calculated, and $I(P,h)$, the average ionization energy deposited at various heights in the atmosphere, is obtained. For energies in the range of 1 GeV–1000 GeV, the ion production in the atmosphere becomes

$$q(h) = \int_{P_c}^{\infty} I(P,h) J(P)\mathrm{d}P, \tag{14}$$

where $I(P,h)$ is the ion pair production at height h, caused by a primary particle with rigidity P. $J(P)$ is the differential cosmic ray rigidity spectrum, which here follows the near–solar minimum observations of the Bess

Table 1. The 26 Strongest FD Events Over the 1987–2007 Period, Sorted by Strength[a]

Order	Date	Decrease (%)	A	$\pm\delta A$	γ
1	31/10/2003	119	229	10/9	-0.87 ± 0.02
2	13/6/1991	87	121	4/4	-0.74 ± 0.01
3	19/1/2005	83	273	16/15	-1.09 ± 0.02
4	13/9/2005	75	233	34/33	-1.07 ± 0.04
5	15/3/1989	70	93	14/12	-0.72 ± 0.06
6	16/7/2000	70	131	7/7	-0.86 ± 0.02
7	12/4/2001	64	153	12/11	-0.96 ± 0.03
8	29/10/1991	56	83	4/4	-0.76 ± 0.02
9	9/7/1991	54	84	4/4	-0.78 ± 0.02
10	29/11/1989	54	173	13/12	-1.08 ± 0.03
11	10/11/2004	53	95	8/8	-0.84 ± 0.04
12	26/9/2001	50	203	16/15	-1.18 ± 0.03
13	25/3/1991	48	82	15/13	-0.82 ± 0.07
14	17/7/2005	47	147	14/13	-1.07 ± 0.04
15	25/9/1998	45	123	45/33	-1.01 ± 0.14
16	27/7/2004	45	97	7/7	-0.91 ± 0.03
17	10/9/1992	44	206	46/38	-1.24 ± 0.09
18	31/5/2003	44	61	3/3	-0.74 ± 0.02
19	25/11/2001	39	75	15/13	-0.87 ± 0.08
20	15/5/2005	38	132	16/14	-1.12 ± 0.05
21	28/8/2001	37	152	15/14	-1.19 ± 0.04
22	27/8/1998	36	38	24/15	-0.63 ± 0.21
23	10/5/1992	35	50	6/5	-0.75 ± 0.05
24	27/2/1992	33	30	2/2	-0.57 ± 0.03
25	18/2/1999	33	38	3/3	-0.66 ± 0.03
26	2/5/1998	28	55	6/5	-0.88 ± 0.04

[a]The first and second columns are, respectively, the order and date of minimum cosmic ray flux. The third column shows the percentage decrease in ion production *relative* to the decrease in cosmic rays from solar maximum to solar minimum over a solar cycle. The final two columns display the parameters A and γ as obtained by the power law fit and defined in equation (6). The decrease from solar maximum to solar minimum, as fitted using equation (6), gives $A_{SC} = 336 \pm 46$ and $\gamma_{SC} = -1.10 \pm 0.04$. It is shown as the black curve of Figure 3. The uncertainty in A is given as an upper uncertainty/lower uncertainty. For example, A for the first event is 229^{+10}_{-9}. Note that no strong FD has occurred after 2007. Date is formatted as day/month/year.

spectrometer [*Sanuki et al.*, 2000]. Thus, any change in ionization during FDs is probed relative to the spectrum close to solar minimum. The change in ionization due to a FD is then given by

$$\delta q(h) = -\int_{P_c}^{\infty} I(P,h) A_k P^{\gamma_k} J(P) \mathrm{d}P. \tag{15}$$

Figure 3 (top) shows the ion production as a function of altitude (see, e.g., *Bazilevskaya et al.* [2008] for comparison with observations). The black thick curve is the ion production at solar minimum estimated by the reference spectrum at solar minimum [*Sanuki et al.*, 2000]. The thin curves are the reduction in ion production relative to the solar minimum spectrum due to each of the 26 FDs based on the fitted A and γ, as given in Table 1. The lowest thin red curve is the exceptional event of October 2003. Using the functional form of equation (6) describing the solar cycle modulation of cosmic rays, one obtains the thick red curve in Figure 3 for the spectrum at solar maximum. Figure 3 (bottom) contains the same information except that the reduction in ion production is normalized here to the reduction from solar maximum to solar minimum, i.e., the difference between the black curve and the red curve at each height h. The ion production is here calculated assuming a cutoff rigidity of 5 GV. Using different values will change the detailed shape of the individual FD curves. Due to the uncertainties in the A and γ parameters, there is also an uncertainty in the derived

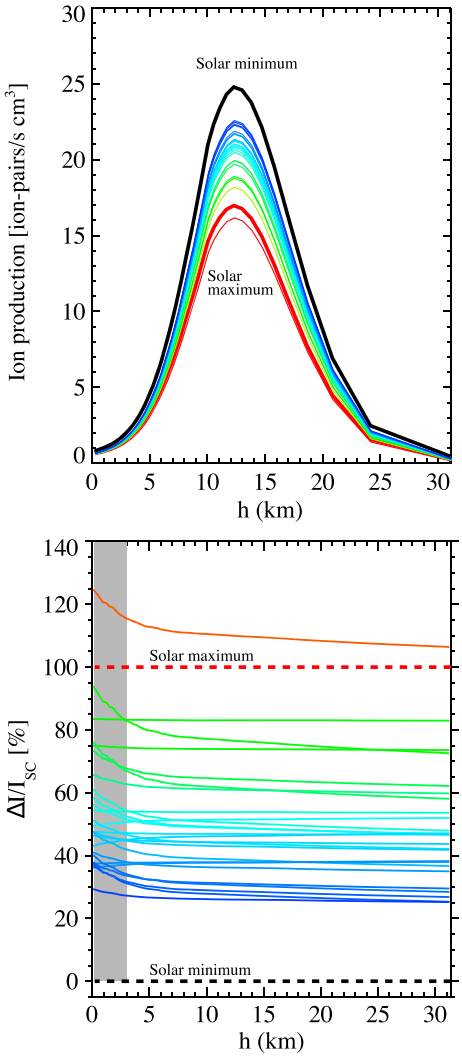

Figure 3. Ion production in the atmosphere. (top) The absolute ion production in a U.S. standard atmosphere as a function of altitude. The thick black curve is the ion production under solar minimum conditions and the thick red curve is during solar maximum, corresponding to latitude of approximately 45° and a cutoff rigidity of 5 GV. The individual thin lines represent the depression relative to the conditions of solar minimum due to the FD events given in Table 1. The lowermost thin red line corresponds to the very strong FD event in October 2003. (bottom) The individual FDs normalized to the solar cycle variation. Solar minimum is given by the thick dashed black line and solar maximum by the thick dashed red line, which in Figure 3 (top) corresponds to the difference between the thick black red curves. Of special interest in this paper are the changes in the lowermost 3 km of the atmosphere here shown as the grey area.

atmospheric ionization, typically ±5% in the *y* axis values in Figure 3 (bottom). This can cause the rankings of the FDs which are close in strength to shift. An improvement that could be made to the model would be to run it for other parts of the globe than the 45° latitude and 5 GV cutoff rigidity we use with the U.S. Standard Atmosphere. This would require using both atmospheres and cutoff rigidities for several latitudes. In section 5.4 we look at the connection between FD strength and response, which gives an indication on whether the rankings are reasonable.

4. Aerosol and Cloud Variations During Forbush Decreases

The main goal in the present work is to study whether FDs have an impact on atmospheric aerosols and clouds. As already mentioned in section 1, a number of studies have looked into this question with diverging conclusions. It is therefore imperative to take a robust statistical approach. In this section such an approach is described.

4.1. Processing Forbush Decrease Time Series

The data under consideration in this study are discrete daily measurements of aerosol or cloud parameters covering a number of years. Any such data series will be denoted $U(t)$, where t enumerates the day. Using all the FDs in Table 1, a collection of FD time series are compiled from $U(t)$ as follows:

1. A FD minimum date t_0 is obtained for FD number i of Table 1.
2. A temporal range encompassing t_0 is set to 36 days, 15 days prior to t_0, and 20 days after, i.e., $U(t)$ with $t = [t_0 - 15, t_0 + 20]$ days.
3. Any linear trend and sample mean is removed over the 36 days. The result is referred to as one FD unit.

The collection of FD units is then denoted $F_i(t)$.

The next step is to reduce the daily data in the days following the FD into a quantifiable measure of a possible response in the different time series. Two such measures are defined below and then also used as a basis for statistical tests.

The growth time of small aerosols into cloud condensation nuclei (CCN) is expected from aerosol dynamics to be within a range of a few days to a maximum of a little more than a week, depending on the rate of aerosol growth [*Kulmala et al.*, 2004]. Thus, when averaging clouds or aerosols over a large area of the Earth, a response in any measured parameter should be correlated in the days following the onset of the FD. This further suggests that an integral over a period of days following the FD should be a good measure of the response. Such a measurement would automatically deal with the autocorrelations in the time series.

The first type of measure is a weighted sum of the FD units, defined as

$$FW(t) = \sum_{i=1}^{N_{\mathrm{FD}}} F_i(t) w_i \tag{16}$$

where w_i are statistical weights with the property that $\sum_{i=1}^{N_{FD}} w_i = 1$, while N_{FD} is the total number of FDs (depending on the temporal range of the particular data set). Three weight distributions are used

$$w_i = \frac{\mathrm{FD}_i(\mathrm{strength})}{\sum_{j=1}^{N_{\mathrm{FD}}} \mathrm{FD}_j(\mathrm{strength})} \tag{17}$$

$$w_i = \begin{cases} \frac{1}{5} & \text{for} \quad i = [1, 2, \cdots, 5] \\ 0 & \text{for} \quad i = [6, 7, \cdots, N_{\mathrm{FD}}] \end{cases} \tag{18}$$

$$w_i = \frac{1}{N_{\mathrm{FD}}} \quad \text{for} \quad i = [1, 2, \cdots, N_{\mathrm{FD}}] \tag{19}$$

The first distribution provides weight according to the derived strength of the FD (Table 1) and includes all FDs. The second distribution provides equal weight to the five strongest FDs and ignores all other. Finally, the third weight distribution gives equal weight to all FDs, strong or weak. Additional weight distributions can of course be applied, but they would not offer notably different information on the significance of any signal which may be found, since the above distribution covers the most extreme range of distribution, from just the strongest to all at equal weights.

The second measurement type is the response defined as the summed signal within the period from day t_1 to day t_2 following the FD minimum, which is the temporal range over which a signal is expected to appear

$$\mathrm{FS} = \sum_{t=t_1}^{t_2} \mathrm{FW}(t). \tag{20}$$

FS is therefore a number. The next step is then to define statistics for the significance of these measurements.

4.2. Bootstrap Samples and Statistical Measures

It is always preferable to minimize the amount of assumptions concerning the nature of any system under examination, as it may end up biasing the result. In situations where the underlying statistical distribution of a variable is simply unknown, the bootstrap method serves as an excellent way to perform distribution-independent statistics. Furthermore, the bootstrap method can also handle issues inherent to time series analysis, such as autocorrelation [*Efron and Tibshirani*, 1994].

The statistical samples are produced and processed in much the same way as the FD time series of section 4.1; however, using random samples from $U(t)$ as follows:

1. A random date t_0 is drawn with replacement.
2. A temporal range encompassing t_0 is set to 36 days, 15 days prior to t_0, and 20 days after, i.e., $U(t)$, where $t = [t_0 - 15, t_0 + 20]$ days.
3. Any linear trend and sample mean is removed over the 36 days. The result is referred to as one sample unit.
4. Steps 1–3 are repeated until a number of sample units corresponding to the number of Forbush decreases (N_{FD}) has been collected. This collection is referred to as a bootstrap sample.
5. The procedure described in steps 1–4 is repeated a number of times, based on the size of the data set being used. The final number of bootstrap samples is N_B, and denoted $B_{i,j}(t)$, where i denotes the sample unit number, and j is the bootstrap sample number.

Note that since each bootstrap sample contains N_{FD} sample units, it is easy to apply the weights of equations (17)–(19) to the bootstrap samples as well. Using the randomly generated $B_{i,j}(t)$, constructs similar to those of section 4.1 can be produced:

$$BW_j(t) = \sum_{i=1}^{N_{FD}} B_{i,j}(t) w_i \tag{21}$$

and

$$BS_j = \sum_{t=t_1}^{t_2} BW_j(t), \tag{22}$$

where index j still indicates the bootstrap sample number. For more information on these constructs, see the previous section.

In the general case it is possible to define the test statistic as the difference between the *measured value time series* and the *expectation values of the N_B bootstrap samples*

$$\mathrm{XFW}(t) = \mathrm{FW}(t) - \frac{1}{N_B} \sum_{j=1}^{N_B} BW_j(t), \tag{23}$$

and for the integrated signal,

$$\mathrm{XFS} = \mathrm{FS} - \frac{1}{N_B} \sum_{j=1}^{N_B} BS_j. \tag{24}$$

In our specific case the two sums (the second terms) in equations (23) and (24) are zero by construction. The question now is whether the above observed values XFW(t) and XFS are drawn from the same distribution as the bootstrap samples, defined as

$$DBW_j(t) = BW_j(t) - \frac{1}{N_B} \sum_{j=1}^{N_B} BW_j(t), \tag{25}$$

and for the integrated signal,

$$DBS_j = BS_j - \frac{1}{N_B} \sum_{n=1}^{N_B} BS_j. \tag{26}$$

This can be answered probabilistically by calculating an achieved significance level (ASL) [*Efron and Tibshirani*, 1994, chapter 15] from the bootstrap samples. The achieved significance for the time series $XFW(t)$ is obtained for each time step over the 36 day period as,

$$\mathrm{ASL}_{\mathrm{boot}}(t) = \left\{ \text{Number of measurements } DBW_j(t) \geq XFW(t) \right\} / N_B. \tag{27}$$

Where t indicates a particular day in the time series and n the index of the bootstrap sample. In the case of the integrated response, *XFS*, the achieved significance level becomes

$$\mathrm{ASL}_{\mathrm{boot}} = \left\{ \text{Number of measurements } DBS_j \geq XFS \right\} / N_B. \tag{28}$$

Such is the basis of the model and $FW(t)$ and *FS* can be readily calculated and their values compared with the empirically determined properties of the distribution function, from identical measurements, $BW_j(t)$ and BS_j, performed on the bootstrap samples.

5. Statistical Test of Atmospheric Data During Forbush Decreases

Here the statistical procedure outlined in the previous section will be applied to the four data sets.

5.1. Forbush Decreases and AERONET Data

The AERONET observations from more than 700 stations are available over the period 1998–present, which spans 17 FDs from the list in Table 1. AERONET data provide information on the transmission of solar radiation from the top of the atmosphere down to the surface at a number of different wavelengths. To quantify the relative blocking of sunlight at different wavelengths, we use here the Angstrom exponent α in the aerosol extinction law, defined through $\tau(\lambda_i) = \tau_1 \lambda^{-\alpha}$, where $\tau(\lambda_i)$ is the aerosol optical thickness at the wavelength λ_i and τ_1 is the approximate optical thickness at $\lambda = 1$ μm. The AERONET data give the fitted exponent $\alpha_{1,2}$ at two wavelengths λ_1 and λ_2 which provide information about the relative abundance of fine aerosols. Long wavelengths respond to their volume fraction, while short wavelengths are more sensitive to the effective radius of the fine mode (<250 nm) aerosol [*Schuster et al.*, 2006]. This motivates us in this study to use the shortest wavelengths at 340 and 440 nm based on the idea that if FDs have an effect on the aerosol production by decreasing nucleation, it should manifest itself as an increase in the effective radius of the aerosols. The measured time series of the Angstrom exponent for the wavelengths 340–440 nm (equation (23) using the weights from equation (18)) is displayed in Figure 4 (top), for the five strongest FDs superposed with even weights. The effect of using different weights is explored in the following sections. It is seen that there is a reduction in the Angstrom exponent in the days following the FD events. The dotted lines denote the one and two sigma deviations (per day) calculated from the bootstrap samples. The hatched area is the period used to integrate the response (day 0 to day 8, where day 0 is the date of the FD minimum stated in Table 1). This period is chosen based on the period during which aerosols can grow to sizes detectable by AERONET, and is expected to be within a week [*Kulmala et al.*, 2004]. Slight variations in the averaging periods used in the paper do not change the conclusions of the paper (see section 7.1). One should note that the AERONET measurements are all performed on land, and here aerosols grow faster than over the remote ocean due to higher condensable vapor pressures over land.

Figure 4 (bottom) shows the integrated values of the bootstrap time series samples as black dot symbols (equation (26)). The red line shows the size of the signal (i.e., calculated using equations (24) and (26)) whose significance is calculated to 98.97%. One complication with the AERONET data is that, apart from a significant signal, it is difficult to quantify exactly how changes in the Angstrom exponent translate into changes in various CCN characteristics.

5.2. Forbush Decreases and SSM/I Data

The SSM/I measures the liquid water content over the oceans, and it is provided in a $1° \times 1°$ grid. Each daily map is an average of the two adjacent days such that when the liquid water content is averaged over the oceans to give a time series, it is effectively a 3 day running average. Figure 5 shows the measured time series (equation (23)) with three different statistical weights applied. In Figure 5a, the weights are based on FD strength (equation (17)). The dotted lines on the left-hand panel represent the significance calculated from the bootstrap samples displayed in equation (25). The corresponding integrated signal as defined by equation (24) from day $t_1 = 3$ to $t_2 = 13$ is shown on the right-hand panel (red line). A different time interval than for the AERONET data is chosen since it is expected that the response of the clouds occurs later than that of the aerosols (see section 7.1). Each point (black dot) corresponds to one integrated response out of the 10^4 bootstrap samples. The significance of the integrated response is 99.68%. Figure 5b is similar to Figure 5a but assumes weights from equation (18). Here the integrated response is significant at the 99.99% level. Figure 5c is similar to Figure 5b except that it considers the five strongest FDs after 1998 (equation (18)), thus allowing a comparison with the AERONET data. The integrated response here is significant at the 99.92% level. Finally, Figure 5d corresponds to all 26 FDs (equation (19)) with equal statistical weights. The integrated response is here significant at the 95.72% level. For all the weights and time intervals considered, a significant reduction in SSM/I liquid water content of clouds over the oceans is seen in the days following FDs. It is also seen that the significance decreases as weaker FDs are added. This can be expected since weak FDs add significant noise without a significant signal.

5.3. Forbush Decreases and ISCCP Data

The data from the Internationale Satellite Cloud Climate Programme (ISCCP) [*Rossow and Schiffer*, 1991] covers the period 1983–2006. Here the D1 data are used, which have global coverage and a 3 h temporal resolution

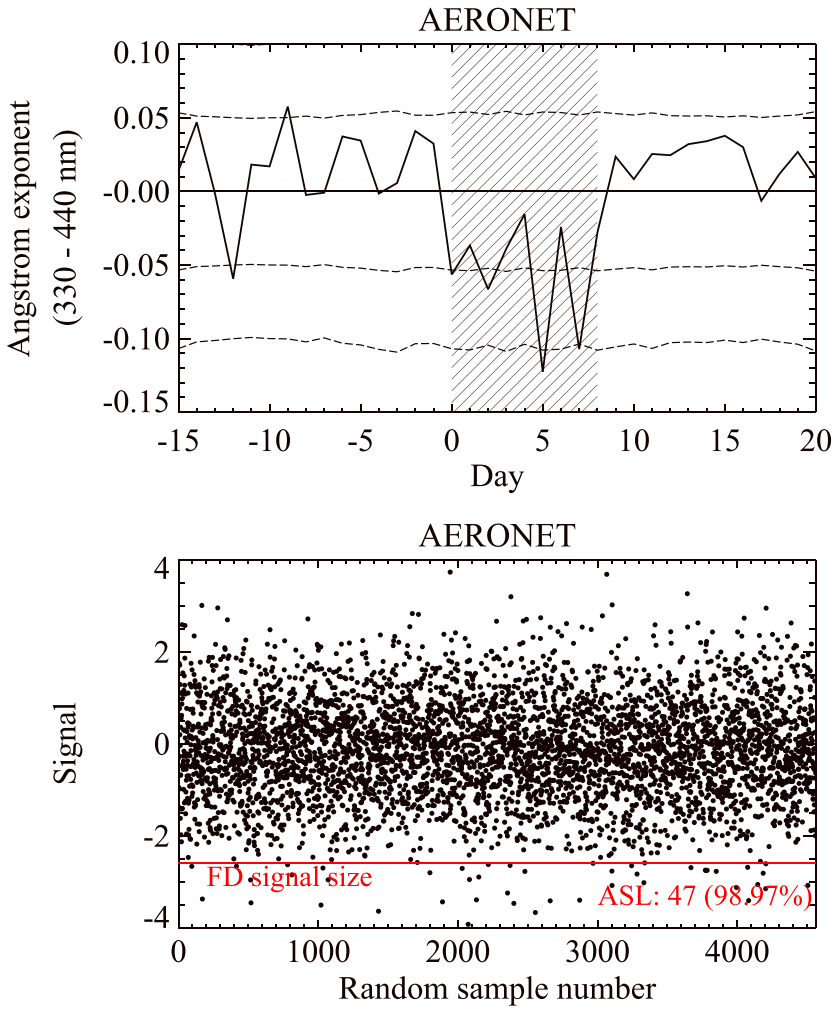

Figure 4. AERONET response to FDs. (top) The superposed FD response in the AERONET data for the five strongest Forbush decreases (after 1998, when the data set starts), 15 days before the minimum in the cosmic ray flux and 20 days after. The dotted lines are one sigma and two sigma obtained using the MC analysis. The hatched area (day 0 to day 8) is the temporal interval used to make the integrated response. (bottom) The integrated interval of each of the bootstrap samples as a black dot. The red horizontal line is the size of the Forbush signal. The response in the integrated signal is at the 98.97% significance level.

(averaged into daily data for this study). Of the parameters offered by the ISCCP, we use both the IR-detected total clouds and the IR-detected low, middle, and high clouds. The IR detection of clouds is used since it has the lowest intrinsic noise compared to the visual channels; moreover, the observation of clouds over the oceans is more accurate and therefore used in the following [*Brest et al.*, 1997]. Figure 6 shows the total IR-detected cloud fraction over the oceans for the three statistical weights. Figure 6a shows the response where the individual FD time series have been weighted with the strength of the FDs. Figure 6b shows the five strongest FDs, while Figure 6c covers the five strongest FDs after 1998, which allows the comparison to the similar figures of the AERONET data and MODIS. Finally, Figure 6d assumes even statistical weights for all 26 FDs. In each of the panels the achieved significance levels for the integrated signal (3–13 days) is stated in the upper left corner.

Figure 7 depicts the signal in all, high, middle, and low IR ISCCP clouds. It is seen that the signal is strongest for the total cloud product, whereas the signal is weaker in the individual cloud layer data sets. The reason for this could be that ISCCP satellites only detects the top of the clouds, and variations in, for example, lower clouds are disturbed by variations in the cloud layer above. This problem will be further discussed in the following section where we analyze the MODIS data.

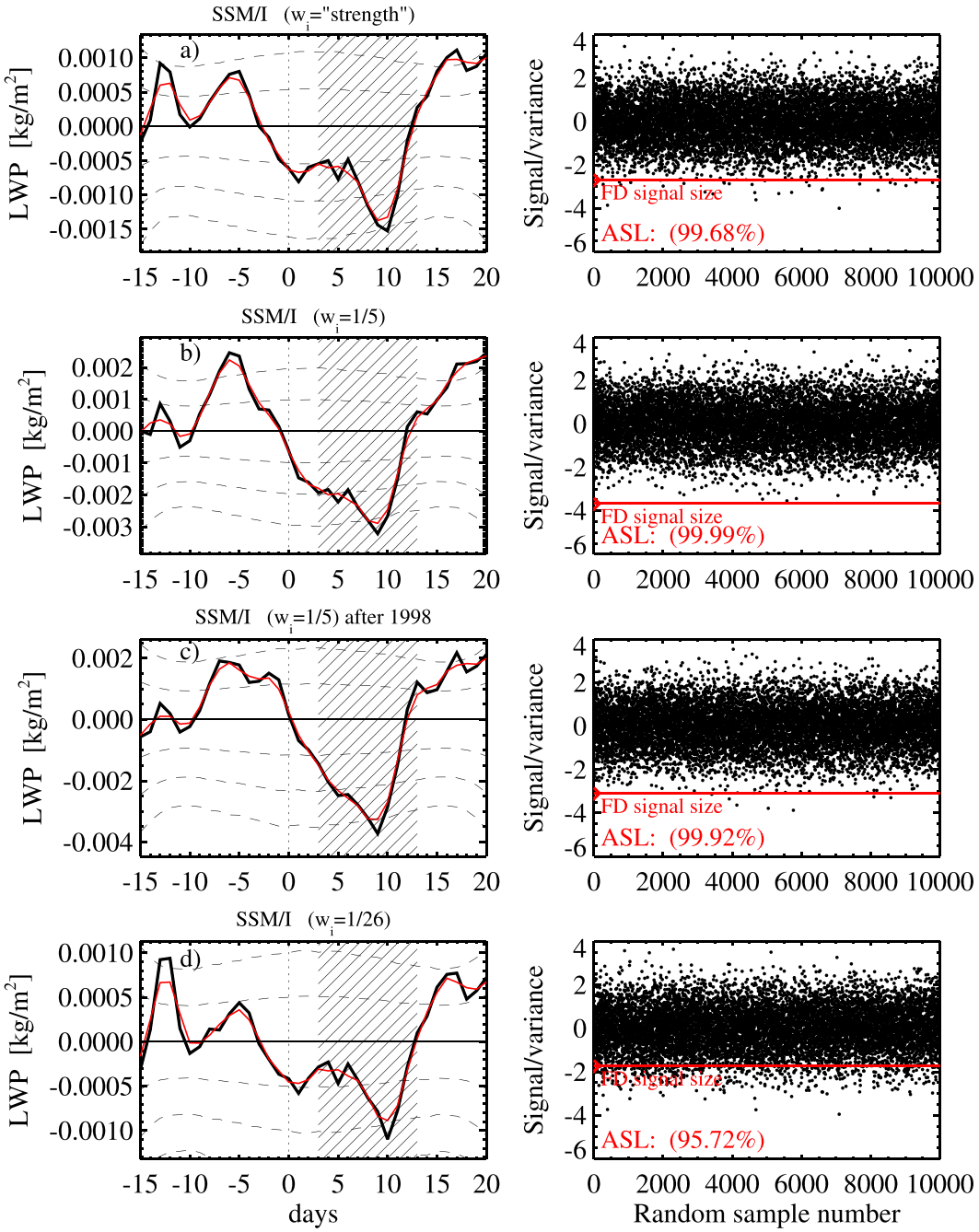

Figure 5. SSM/I data of liquid water content over the oceans. (left column) Superposition of SSM/I data using the strength of the FDs as (a) statistical weights (equation (17)) and (b) equal weights for the five strongest FDs (equation (18)). (c) Similar to Figure 5b, but using only the five strongest FDs after 1998, and (d) uses equal weights for all FDs (equation (19)). The red curve is a 3 day smoothing of the daily data. The hatched area denotes the temporal interval used to integrate the response (3–13 days). The dotted lines are 1, 2, and 3 standard deviations obtained using the MC bootstrap analysis. (right column) The bootstrap samples of the integrated signal. The abscissa is the bootstrap sample number and the ordinate is the size of the integrated bootstrap signal using the different statistical weights corresponding to the different rows. The red lines mark the size of the real FD signal with the corresponding weight. The achieved significance levels from top to bottom are 99.68%, 99.99%, 99.92%, and 95.72%.

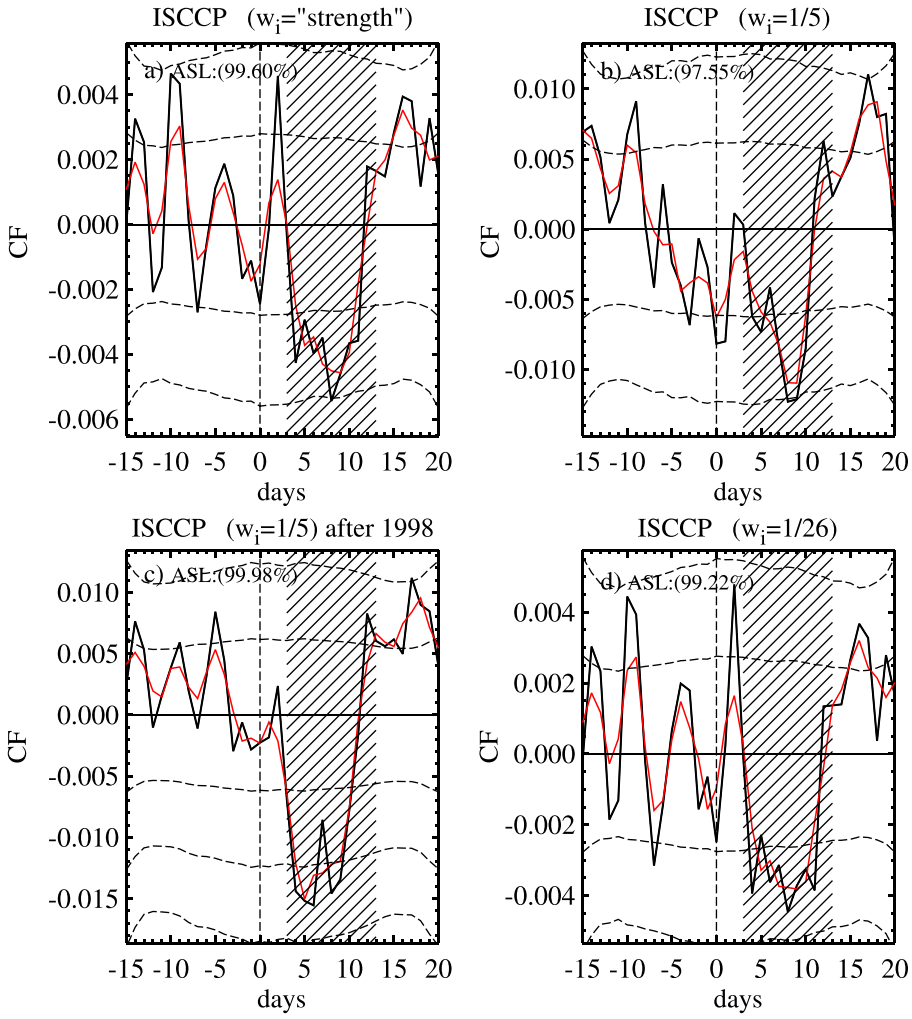

Figure 6. Statistics of the total IR-detected ISCCP clouds over the oceans. (a) The variation in the total IR-detected clouds averaged over the oceans using the strength of the FDs as statistical weights. (b) The five strongest FD (see, Table 1), (c) the five strongest FDs after 1998 (see, Table 1). (d) Based on even statistical weights for all the 26 FDs. The black curves denote the change in the response of the total IR cloud fraction, while the red curve is a 3 day smoothed version of the black curve. The hatched areas denote the temporal interval used to integrate the response (3–13 days), with the achieved significance levels stated in each panel. The dotted lines are 1, 2, and 3 standard deviations obtained using the MC bootstrap analysis.

Note that there is a discrepancy between Figure 7a and Figure 1d from *Svensmark et al.* [2009] which also depicts total IR-detected ISCCP clouds. This is because Figure 1d from *Svensmark et al.* [2009] only includes data between 40° northern and 40° southern latitude.

5.4. Forbush Decreases and MODIS Data

From "MOD08_D3" (the data product can be found on the MODIS website) we chose the parameters listed in section 2.3. The chosen parameters and their MODIS names are shown in Table 2. The daily average maps given by the data product cover all of Earth, and from these maps we produce global daily means for each of the parameters. The CCN product is ocean only due to difficulties with retrieval of aerosol counts over land [*Levy et al.*, 2010]. Details on how the CCN product is derived can be seen in *Remer et al.* [2005].

Figure 8 displays the result of the statistical test in the case of the five strongest FDs, in the period after MODIS data are available, starting with the event on 16 July 2000 (note that there are no strong FDs between 1998 and 2000, so these are the same FDs as in the AERONET analysis). The panels show the time series as defined in equation (16) for each of the above parameters using the weights in equation (18). The decreases in ϵ, τ, LWP, and CF as well as the increase in R_{eff} extend beyond the 95% level. Figure 8 and Figure 1c of

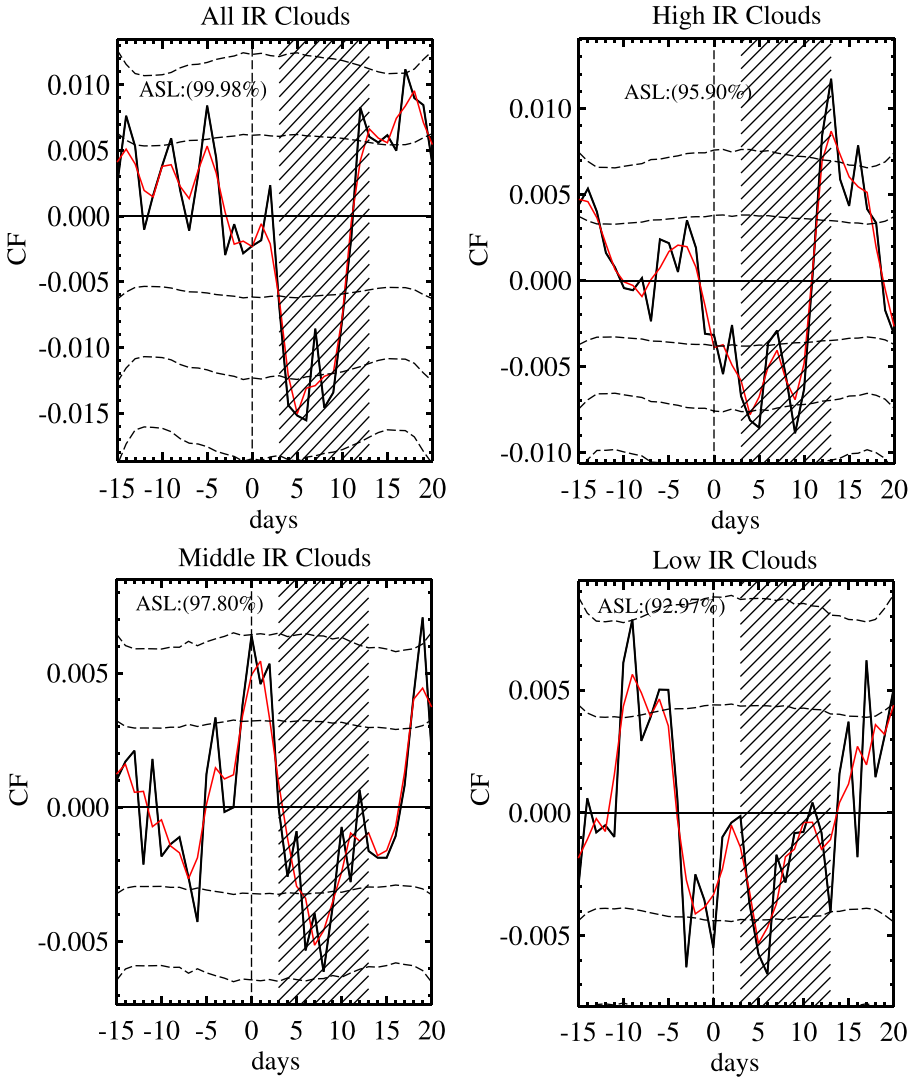

Figure 7. Statistics of IR-detected ISCCP cloud fractions averaged over the oceans for the five strongest FD after 1998. The red curve is a 3 day smoothing of the daily data. (top left) All IR-detected clouds. (top right) High clouds. (bottom left) Middle clouds. (bottom right) Low clouds. The hatched area denotes the temporal interval used to integrate the response (3–13 days) and the achieved significance levels are stated in each panel. The dotted lines are 1, 2, and 3 standard deviations obtained using the MC bootstrap analysis.

Table 2. Parameters and Their Name in the "MOD08_D3" Data Product[a]

Parameter	MODIS "MOD08_D3" Parameter Name
ϵ (-)	Cloud_Effective_Emissivity_Mean
CCN (10^8 cm^{-2})	Cloud_Condensation_Nuclei_Ocean_Mean
τ (-)	Cloud_Optical_Thickness_Liquid_Mean
LWP (gm^{-2})	Cloud_Water_Path_Liquid_Mean
CF (-)	Cloud_Fraction_Liquid_Mean
R_{eff} (μm)	Cloud_Effective_Radius_Liquid_Mean

[a]Epsilon is the effective long-wave emissivity of clouds, equivalent to one minus the transmissivity. Epsilon is dimensionless. CCN (Cloud Condensation Nuclei) are aerosols in the size range 50–100 nm on which water vapor condenses to form cloud droplets. MODIS measures the column density of CCN in units of cm^{-2}. Tau is cloud optical thickness and is given by the integrated extinction coefficient over a vertical column of unit cross section. Tau is dimensionless. LWP is measure of the mass of liquid water droplets in the atmosphere above a unit surface area. LWP is in units of g m^{-2}. CF or cloud fraction is the fraction of each pixel in satellite imagery that is covered with clouds. CF is dimensionless. Finally, R_{eff} is the cloud drop effective radius a weighted mean of the cloud drop distribution. R_{eff} has the dimension μm.

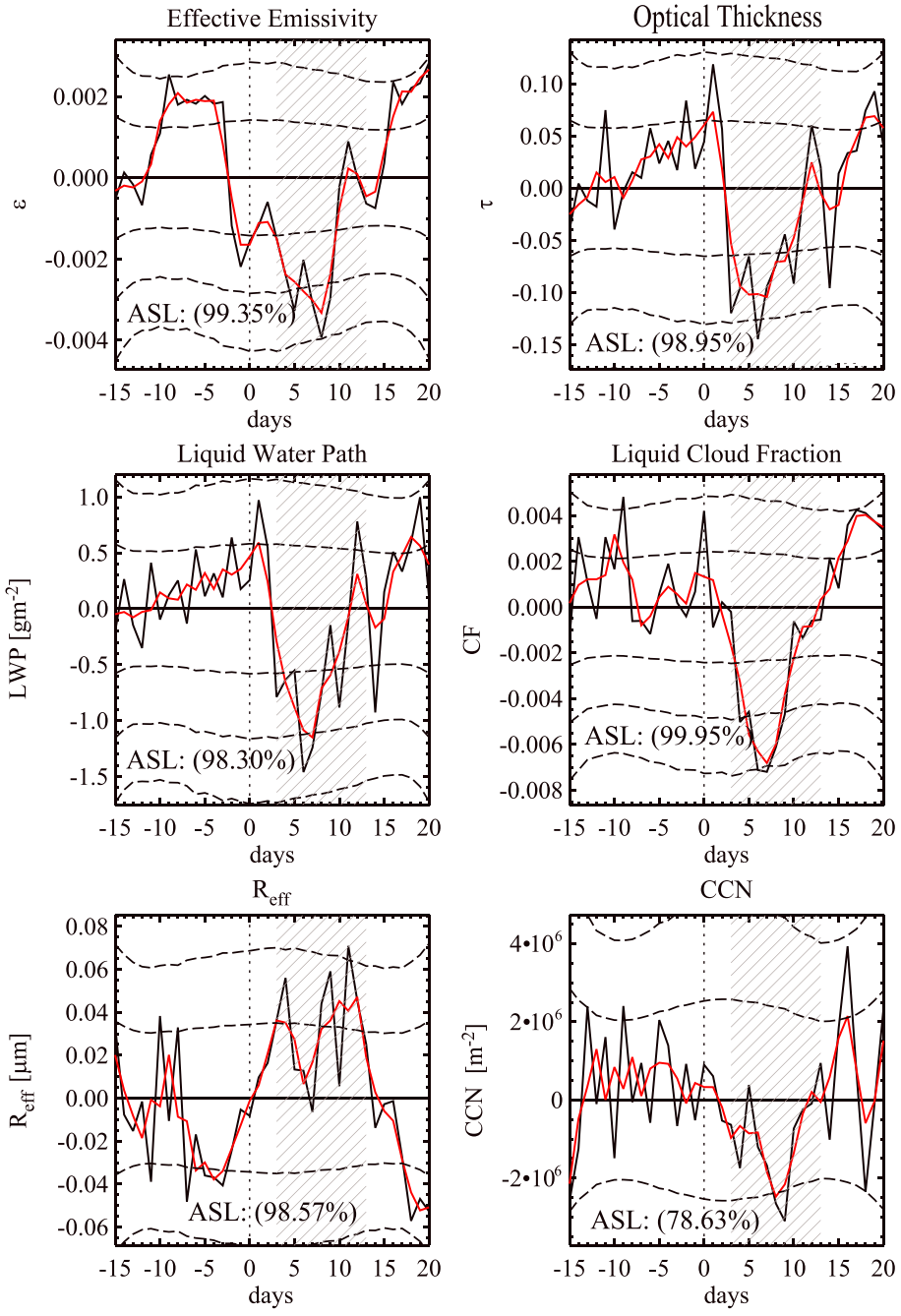

Figure 8. MODIS global daily means of the parameters ϵ, τ, CF, CCN, LWP, and R_{eff} averaged for the strongest five Forbush decreases from year 2000 and onward (Table 1). The black curve is the response in the cloud parameter, while the red curve denotes a 3 day smoothed version of the black curve. The dotted lines are 1, 2, and 3σ significance levels. The hatched area is the temporal range used to integrate the response, and the achieved significance levels (ASL) for this measure is stated on each figure (see section 4).

Svensmark et al. [2009] both depict the liquid CF as measured by MODIS but differ slightly in shape because *Svensmark et al.* [2009] treated "CF = 0" values as missing data; an issue that has been corrected in the present work.

Six days after the FD minimum, the parameters LWP, τ, and CF reach their minimum values, compared to ϵ which takes 8 days to reach minimum value. At day 9 the minimum for CCN is reached; however, it is less than 80% significant. The effective radius (R_{eff}) reaches its maximum after 11 days. The days when the parameters

Table 3. List of Quantities for the Six MODIS Parameters Using Data From FDs 1–5[a]

Parameter	Reference Level$\pm\sigma$	ΔP_{meas}(%)	ΔP_{der} (%)	Extremum (days)
ϵ (-)	0.686±0.003	−1.29	−1.7±0.78 [30]	7.7±4.5
CCN (10^8 cm^{-2})	2.60±0.06	−3.32	−2.5±5.3 [32]	6.1±4.0
τ (-)	11.09±0.12	−2.87	−3.7±1.5 [31]	8.1±4.5
LWP (gm^{-2})	108.60±1.11	−3.05	−2.2±1.6 [31]	8.5±4.1
CF (-)	0.277±0.004	−5.53	–	9.5±4.3
R_{eff} [μm]	16.95 ± 0.07	0.71	−0.19 ±2.1[31]	6.9 ± 4.3

[a]Shown is reference level, percentage change ΔP_{meas}, derived change ΔP_{der}, (where P is the parameter in question), estimated from equations (30), (31), and (32) (the equation used for each parameter is indicated by the number in the bracket), the level of significance for the signal, and the day where the extremum occurred. Note that the extremum days for the values in the table are slightly different from those in Figure 8 (and the text). The reason is that in the figure the average is made from the ensemble of the five events, while in this table the average of the five individual events is shown.

reach their extremum values when the average of the five strongest individual events is used, are shown in column 5 of Table 3. The ASL of integrated responses, using equation (28) from days 3 to 13 following the FD, is displayed in each of the figures for the six parameters in Figure 8. It is seen that all FD signals are significant at the 98% level or better, except for the CCN parameter, which will be discussed in section 6.

We quantify the connection between Forbush decrease strength and parameter response for each of the MODIS parameters, in the same way as was done for the ISCCP (low clouds), MODIS (liquid clouds), AERONET (Angstrom exponent 330–440 nm), and SSM/I (liquid water path) data sets in *Svensmark et al.* [2009]. As the independent variable, we use the percentage change in ionization as listed in Table 1 for all of the FD events. The corresponding dependent variable is defined as a percentage change ($\Delta P_{w(i)}$) in $P_w(t)_i$, where i refers to one of the six cloud parameters, and $\Delta P_{w(i)}$ is the difference between the mean and the extremum value between days 0 and 15 of the FD. Minima in the data sets were used for all parameters except for the effective radius (R_{eff}) where maxima were used.

Figure 9 shows the resulting scatterplots for all of the six parameters, together with least squares linear fits and LOESS regression. FD 1, farthest to the right on the plots, is an outlier which can perhaps be understood since the FD happened at the same time as the Halloween event of 2003, which contained eleven X class solar flares during the 18 days of the event [*Woods et al.*, 2004].

Student's t test is used in order to determine if the fitted slopes are statistically different from zero. The significance of the slope of ϵ is 98% (99% excluding FD 1), for LWP it is 95%, for CF 95% (90% excluding FD 1), R_{eff} 95% excluding FD 1 and insignificant when including it, and for τ it is 95% (99% excluding FD 1). Regarding CCN the slope is significant at the 90% level when FD 1 is excluded, and it is insignificant when including it. If the reverse analysis is carried out, i.e., looking for minima in R_{eff} and maxima for the other parameters, we find that the probability for the slopes to be different from zero to be insignificant, which indicates that the result is not due to a symmetric increase in the level of fluctuations. So when the GCR influx decreases, it is followed by a decrease in ϵ, CF, LWP, and τ and possibly an increase in R_{eff}. Note that this result does not necessarily imply that the relation is strictly linear, it merely suggests that there is a connection between the strength of the FD and the cloud parameter response. The LOESS results also shown in Figure 9 illustrate that the relation is not completely linear.

The results in the last part of section 5.3 on the ISCCP data do not provide a clear answer to where in the atmosphere the effect can be seen. Returning to this question with the MODIS data, we now look at the division between ice clouds fraction and liquid cloud fraction. Figure 10 demonstrates that the signal is almost exclusively seen in liquid clouds. MODIS uses a number of near-infrared and visible channels to determine the cloud thermodynamic phase, i.e., if a cloud region consists of liquid or ice particles [*Platnick et al.*, 2003]. The combined signal (ice + liquid + undetermined clouds) in Figure 10a shows a clear response to FDs. However, if the plot is divided into the subtypes ice and liquid clouds (Figures 10b and 10c, respectively), then it is clear that the response originates from the liquid cloud fraction, which is consistent with the strong signal also seen

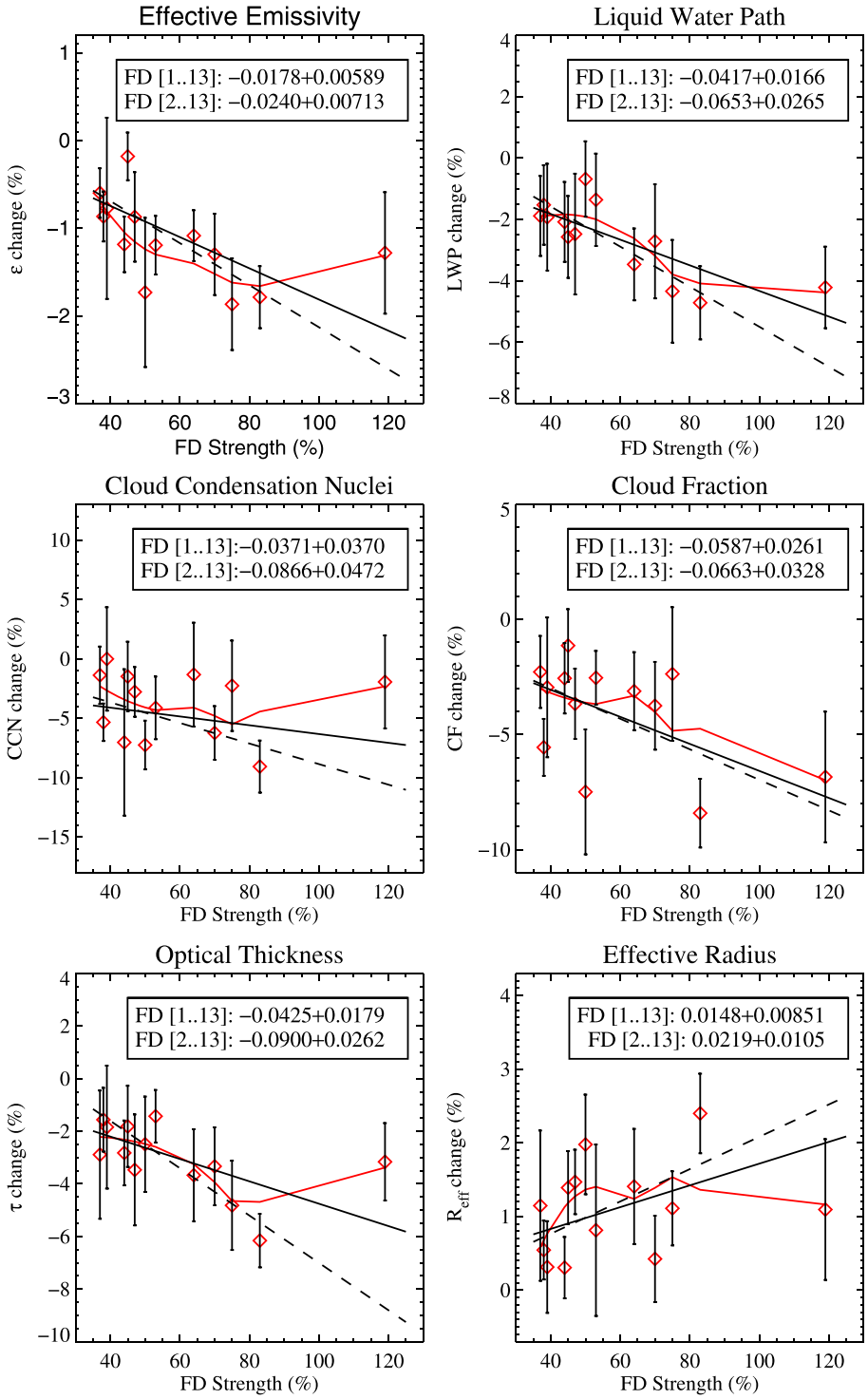

Figure 9. The Forbush decrease strength (from Table 6) and response in six MODIS cloud parameters. The black lines are weighted linear trends of the data points. Slope values and standard deviations of the slope are written on each plot. The broken lines show the same trend, except that the data point for the extreme Halloween Event (FD 1) has been excluded. Although linear fits are used to permit a *t* test, this does not mean that the relationship is necessarily linear. To illustrate this we have also added a LOESS regression (red lines) using a second-order polynomial and a 0.8 fraction of the total points in each local regression. Also note that equivalent figures for the ISCCP, SSM/I, and AERONET data have already been published in *Svensmark et al.* [2009] using the same list of FDs.

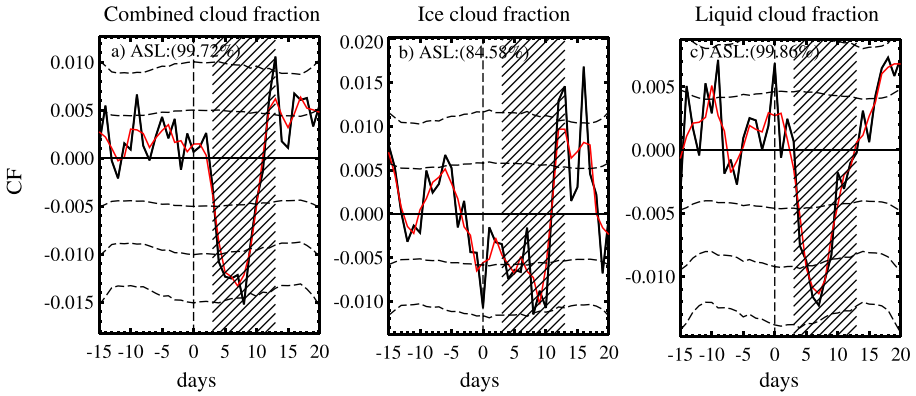

Figure 10. Response in MODIS-derived cloud fractions by type, to the five strongest FDs from year 2000 and onward. (a) Cloud fraction combined. (b) Ice cloud fraction. (c) Liquid cloud fraction. The red curve is a 3 day smoothing of the daily data. The hatched area denotes the temporal interval used to integrate the response (3–13 days). The dotted lines are 1, 2, and 3 standard deviations obtained using the MC bootstrap analysis.

in Figure 7 (top left) in the ISCCP All IR-detected clouds. Note that in the study by *Marsh and Svensmark* [2000] the response in clouds to the 11 year solar cycle was clearly strongest for low clouds. In contrast, the present study can only confirm that the short-term FD response is seen in liquid clouds, possibly due to the reasons mentioned in section 5.3.

5.5. Intercorrelation in MODIS Data

A possible issue with multiparameter analysis is intercorrelation, which can lead to overestimating the significance of simultaneous signals in the investigated parameters. Causes for intercorrelation could be if parameters are used to derive each other or if some of the same optical channels on the instruments are used to measure multiple parameters. For instance, liquid water path is derived from optical thickness and effective radius [*King et al.*, 1997, page 65], although effective radius and optical thickness are measured using different wave bands, as seen in Table 1 [*King et al.*, 1997]. The intercorrelations between the six investigated MODIS parameters are shown in Figure 11. The highest correlation found is between liquid water path and optical thickness ($r = 0.88$) which could be expected since one is derived from the other, as described above. Looking at the panels of those two parameters in Figure 8, they also appear quite similar. The only other two parameters that have a correlation coefficient (r) above 0.5 is emissivity and cloud fraction.

5.6. Principal Components Analysis

To combine the information from several data sets we perform a principal components analysis (PCA) on the eight cloud parameter time series, namely, the six MODIS parameters, the ISCCP total IR clouds over oceans, and SSM/I. The PCA procedure constructs an orthogonal transformation matrix, defining (up to) eight new time series as linear combinations of the original eight as projections onto the new basis. The first principal axis is chosen to account for the highest possible amount of variance in the system, and the projection of the time series data along this direction referred to as the first principal component (PC). (The second principal axis accounts for the second most amount of variance, projections onto it provides the second principal component, and so on). The first PC can be interpreted as a measure of the total change in the cloud system during the five strongest events in the period starting with the FD on 16 July 2000. To use the PCA procedure, all parameters were normalized by subtracting the mean value, removing the linear trend, and finally dividing by the standard deviation of the time interval. The first PC is

$$\begin{aligned} \mathrm{PC1}(t) = {} & 0.38\epsilon(t) + 0.26[\mathrm{CCN}](t) + 0.37\tau(t) + \\ & 0.35[\mathrm{LWP}](t) + 0.39[\mathrm{CF}](t) - 0.29R_{\mathrm{eff}}(t) + \\ & 0.39[\mathrm{CF}](t) + 0.39[\mathrm{ISCCP}](t) + \\ & 0.41[\mathrm{SSM/I}](t) \end{aligned} \tag{29}$$

where the numerical coefficients are the first eigenvector of the correlation matrix which can be seen as the amount of variance in the time series with multiple variables [*Miller and Miller*, 2000, chapter 8]. The six MODIS parameters can be seen in Figure 8, the ISCCP parameter in Figure 7 (top left), and finally the SSM/I parameter in Figure 5c.

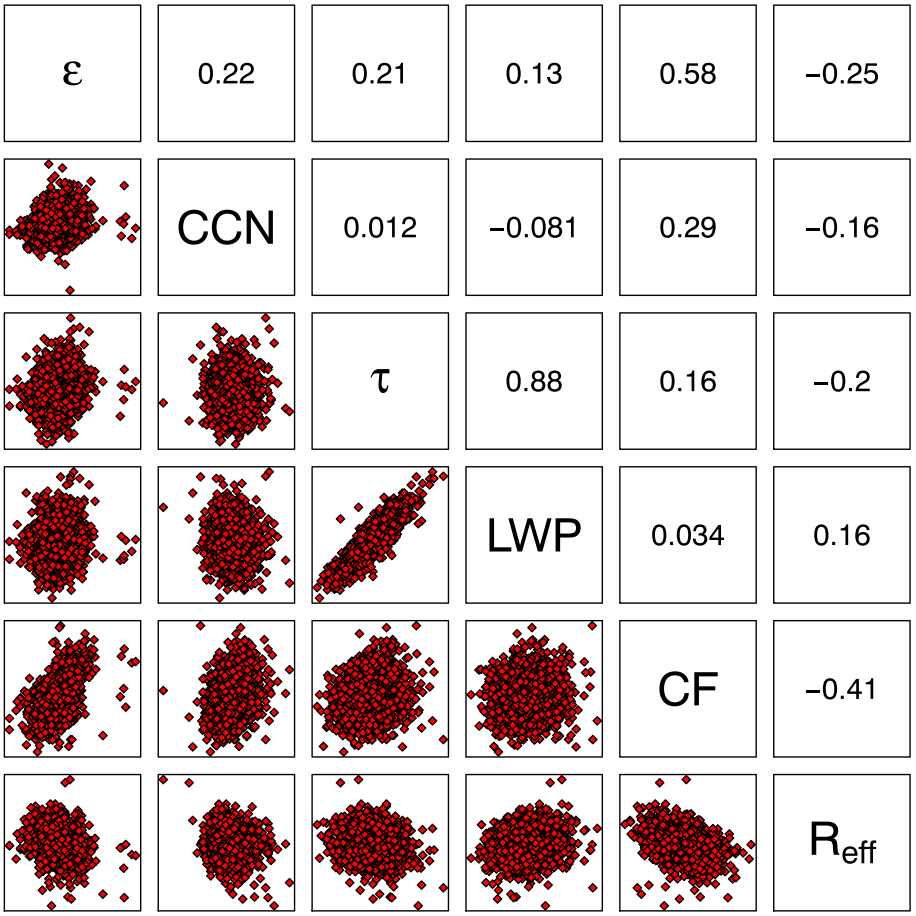

Figure 11. Intercorrelation of the six MODIS parameters. Below the diagonal from top left to bottom right, correlation plots are shown. Above the diagonal the correlation coefficients corresponding to the plots are shown. Data points above five sigma have been filtered from the data in order to avoid distortion from unphysical events (instrumentation errors). Furthermore, seasonal variations were removed by filtering the data with a Fourier filter, removing variations greater than 90 days.

Figure 12 presents the first principal component over the 36 day period. The variance is determined by Monte Carlo sampling using random time series for each of the eight parameters and then calculating their first PCs follow. The standard deviation is calculated from these realizations. A clear minimum is seen at days 5 and 6, which demonstrates that a signal in the cloud parametric system is simultaneously found in all (or most) parameters. Integrating the response from days 3 to 13 and comparing with Monte Carlo realizations, it is found that none of the 10^4 realizations can display a similar large integrated signal, and the ASL > 99.99%. This is the case even if the absolute values of the area is used. It is also important to note that the sign of the components of the first PC is found to have the R_{eff} parameter with a sign opposite to all the other parameters. This is precisely predicted by cloud physics (see next section), and the probability of having this particular sign relation for the eight parameters from a random realization is even more unlikely than any of the isolated calculated significance levels. The CCN parameter from the MODIS data contributes with low variance to the first PC and its sign is wrong; however, as will be discussed in the next section, the CCN signal is expected to be unobservable due to the high noise level of the MODIS CCN data product. Due to the intercorrelation between liquid water path and optical thickness in the MODIS data, it could be argued that only one of these parameters should be used, but we include both for the sake of completeness, and since they are also both included in the MC analysis the significance should not be affected artificially by this. In summary, the PCA appears to strengthen the conclusion that the cloud system is actually disturbed when FD events occur.

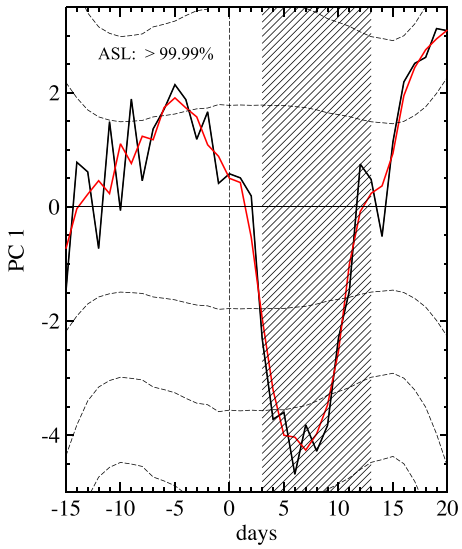

Figure 12. The first principal component (based on the six MODIS parameters, ISCCP total IR clouds over oceans and SSM/I) averaged over the five strongest events in the period starting with the FD on 16 July 2000. The dashed lines show 1 and 2 standard deviations. The hatched area from days 3 to 13 is the interval over which first principal component is integrated. The achieved significance level from the integrated signal here is >99.99%, meaning that none of the 10^4 Monte Carlo realizations gave an absolute result of the same size or larger.

6. Estimated and Observed Changes in Cloud Parameters

We now turn to the physics of the measured changes in the observed parameters and calculate whether the changes are within the expected range. Based on observations of the energy entering the oceans over a solar cycle, a peak to peak variation of 1–1.5 W/m^2 is found in the radiative budget [*Shaviv*, 2008; *Howard et al.*, 2015]. This change has been associated with an absolute change of ≈2% in low cloud fraction (corresponding to an ≈5% relative change in low cloud fraction). Since the effect of the largest FDs is only slightly smaller than a solar cycle variation, as seen in Figure 3, the expected variation during the strong FDs is also of the order of 1–2 percentage points (or possibly smaller, since the effect in total liquid clouds may be smaller than that in low clouds alone). The question is how large such a signal is compared with the intrinsic noise of the various data sets.

Column 2 of Table 3 lists the reference levels of the six MODIS parameters, and the mean percentage changes during the five largest events are shown in Column 3. We define the reference level according to equation (4), and the percentage change relative to the reference using the extremum value within days 3 and 13. Now we want to check if the magnitude of changes in the MODIS parameters are internally consistent and if we would expect to see a signal at all, considering the noise in the data. To test this we used a series of equations from *Stephens* [1978] (equation (30)) and Chapter 2 of *Hobbs* [1993] (equations (31)–(32)):

$$\epsilon = 1 - e^{-a_0 \mathrm{LWP}}, \tag{30}$$

$$\tau \approx \frac{3}{2\rho}\frac{\mathrm{LWP}}{R_{\mathrm{eff}}}, \tag{31}$$

$$\tau \approx 2.4\left(\frac{\mathrm{LWP}}{\rho}\right)^{2/3}\left(N_c\right)^{1/3}. \tag{32}$$

Here a_0 is a scaling parameter which is found from the MODIS data by using reference levels for ϵ and LWP and then solving for a_0, ρ is the density of water (1000 kg m^{-3}), and N_c is the droplet column density where CCN is used as an approximation.

Using these equations we can then take a given change in one of the MODIS parameters and calculate the magnitude of change we would expect in some of the other parameters, the derived percentage change (ΔP_{der}).

Table 4. Mean, Noise, and Signal Levels for the Four Data Sets Using the Five Strongest FDs Evenly Weighted Time Series[a]

Observational Platform	Parameter	Mean Value	Noise Level	Noise Level (%)	Signal Size (%)	Signal/Noise
MODIS	Liquid cloud fraction	0.355 (-)	0.005 (-)	1.5	3	2.0
ISCCP	All IR cloud fraction over oceans	0.64 (-)	0.006 (-)	0.9	2.3	2.6
ISCCP	Low cloud fraction over oceans	0.32 (-)	0.008 (-)	2.5	2.5	1.0
SSM/I	Liquid water path	0.090 (kg/m^2)	0.001 (kg/m^2)	1.1	3.3	3.0
AERONET	Angstrom exponent	1.25 (-)	0.05 (-)	5	8	1.6

[a]The mean is here defined as the mean of the entire 36 day interval, and the noise level is the MC-based standard deviation on the day that the extremum signal occurs. It is seen that the noise level is the smallest for the ISCCP All IR cloud and SSM/I data followed by the MODIS and AERONET data. ISCCP low IR cloud data are least likely to resolve a signal.

ΔP_{der} is found for each parameter using the reference levels (as seen in Table 3) of the parameters they can be calculated from along with corresponding changes during a FD. For example, for τ,

$$\tau_a = \frac{3}{2\rho}\frac{\mathrm{LWP}}{R_{\mathrm{eff}}},$$

$$\tau_b = \frac{3}{2\rho}\frac{\mathrm{LWP} + \Delta\mathrm{LWP}}{R_{\mathrm{eff}} + \Delta R_{\mathrm{eff}}},$$

$$\Delta\tau_{\mathrm{der}} = \frac{\tau_b - \tau_a}{\tau_a} \times 100\% = -3.73 \pm 1.54\%.$$

The calculated ΔP_{der} for all parameters is shown in Table 3. Note that the measured percentage drop of −2.87% for τ lies within the uncertainty of the derived value.

Using equation (32) the derived change for N_c is found to be $\Delta N_{c,der} = -2.5 \pm 5.3\%$. With the assumption that CCN changes as N_c, ΔCCN_{der} is within one sigma of the CCN data from Figure 8. The lack of significant CCN signals in Figures 8 and 9 can possibly be explained by the fact that the expected change is smaller than the noise. Similarly, $\Delta R_{eff,der}$ is also contained in the noise.

For LWP, ϵ, and τ the observations and derived parametric changes appear to be consistent, and this remains the case for parameters where several of the equations ((30)–(32)) could be used to derive ΔP_{der}. Table 3 summarizes the results.

Turning to the observed extremum variation in the other data (SSM/I, ISCCP, and AERONET), Table 4 summarizes the observed mean values and the extremum change in percent following the five strongest FD. Also shown are the standard deviation of the fluctuations in percent of the mean value. The signal-to-noise ratio is estimated from these values, from which one can see that the SSM/I has the largest signal-to-noise ratio, whereas the ISCCP IR low clouds have the smallest ratio.

7. Discussion

The fundamental question addressed here and in previous analyses is whether a real physical response exists in the aerosols and cloud parameters in the days following Forbush decreases. By ranking FD events according to their impact on the ionization in the lower atmosphere (Table 1), it was possible to test not just the atmospheric response to FD but also the size of the response as a function of the FD strength.

The test for significance was performed using a Monte Carlo bootstrap statistical procedure defined in section 4. A significant signal was found in all of the four independent data sets in the days following the FD minimum (AERONET, SSM/I, ISCCP total IR clouds, and all MODIS parameters except for the MODIS CCN parameter, which, however, is expected based on its inherent noise level). Second, applying the Monte Carlo bootstrap statistical method by integrating the response in the days following the FDs leads to high statistical significance of the observed responses. Achieved significance for the five strongest FDs after 1998 are, AERONET: 98.97 (Angstrom exponent), SSM/I: 99.92% (liquid water content), ISCCP: 99.98% (All IR cloud fraction), and MODIS CF: 99.90% (liquid cloud fraction). The integrated response automatically addresses autocorrelations in the data sets.

Equally important is that the numerical changes in the different cloud parameters are found to be consistent with the expected changes in the physics of aerosols and clouds as discussed in section 6. The consistent chain of reactions is fewer cosmic rays → less ionization → less aerosol nucleation, fewer formed CCN → fewer cloud droplets → larger cloud droplets [*Boucher et al.*, 2013], decrease in cloud fraction, cloud optical thickness, and in cloud emissivity. Finally, since the droplets are larger, their rainout is more effective and it is consistent with the reduction in liquid water content.

Furthermore, the atmospheric responses are found to scale with the strength of the FD, as seen in Figure 9. One sees that the signals are weaker for the less powerful FDs, suggesting that the response of the weak FDs is dominated by noise as could be expected. A likely reason is that the ionization and other average cloud parameters are fluctuating due to meteorological changes, and thus mask the effect of small FDs. The errors in the estimation of FD strength can also play a part in masking an effect from the weaker FDs.

7.1. Signal Delay

The time between the FD and the extremum of the response in the cloud parameters is referred to as the signal delay. For the cloud data sets investigated in this study the signal delay is consistently between 6 and 11 days (see also *Svensmark et al.* [2009]). If the mechanism behind the changes is due to effects of ionization on the nucleation and growth of aerosols, it is expected that there would be a substantial signal delay as several processes would have to happen before a signal would be visible in the cloud data. The first step is that freshly nucleated aerosols (about 1 nm in size) would have to grow to CCN sizes, which is up to ~100 nm depending on atmospheric conditions. A growth rate for aerosols in the order of 1 nm h^{-1} is not uncommon [*Kulmala et al.*, 2004], which can explain a signal delay of several days, such as is seen in the AERONET data (section 5.1). The second step is that the CCN-sized aerosols have to activate in order to grow into cloud drops, and furthermore. the new drop concentration (and size distribution) will affect the clouds through, e.g., rain out if there is fewer (and therefore larger) cloud drops. Adding up these steps, it is thus not unreasonable to observe a signal delay of about a week. We thus choose days 3 to 13 as the time period where a signal can be expected, for the cloud data sets. Varying this by 1 to 2 days in either direction can cause some change in the signal, but not in a way that changes the overall conclusions.

Note that if the above response is caused by a decrease in aerosol nucleation and subsequent response in CCNs, it would seem to go against the common theory as implemented in large global aerosol models [e.g., *Snow-Kropla et al.*, 2011]. In such models, any small change in the formation of new aerosol particles (caused by, for example, a change in ions) vanishes before growth to CCN sizes can be reached. Thus, if ions are responsible for the observed changes in the present analysis, then ion effects in current atmospheric models are underrepresented.

7.2. Ultra Violet and Total Solar Irradiance

Although the above results are consistent with a cosmic ray/atmospheric ionization link, effects on cloud cover could also arise from sensitivity to changes in the UV and/or the Total Solar Irradiance (TSI). Traditionally, it has been difficult to attribute cloud changes to one process or the other [*Boucher et al.*, 2013; *Laken et al.*, 2011], so in this section we investigate a possible UV and/or TSI effect.

7.2.1. Ultra Violet Irradiance

Changes in the UV range are important for photochemistry in the atmosphere, and they could therefore influence aerosol formation and cloud microphysics. As a consequence, it is not unreasonable that a simultaneous change in relevant UV wavelengths during FDs could explain the change in aerosols and clouds. This is especially so as one of the most important trace gases for aerosol nucleation and growth is sulfuric acid. Thus, a decrease in the UV frequencies concurrent with the FDs would lead to less sulfuric acid, fewer nucleated particles, and slower growth. The following photochemical reaction

$$O_3 + h\nu \rightarrow O_2 + O(1D) \tag{33}$$

where $h\nu$ represents a photon, initiates most of the sulfuric acid production since O(1D) produces the OH radical, which reacts with SO_2 to form sulfuric acid. The photolysis constant can be calculated from

$$J(O_3 + \gamma \rightarrow O_2 + O(1D), t) = \int_0^\infty S(\lambda, t)\tau(\lambda)\sigma(\lambda)Y(\lambda)\mathrm{d}\lambda \tag{34}$$

where λ is the wavelength, t time, $S(\lambda, t)$ is the solar spectrum at the top of the atmosphere, $\tau(\lambda)$ is the transmission through the atmosphere, $\sigma(\lambda)$ is the cross section, and finally, $Y(\lambda)$ is the quantum yield function.

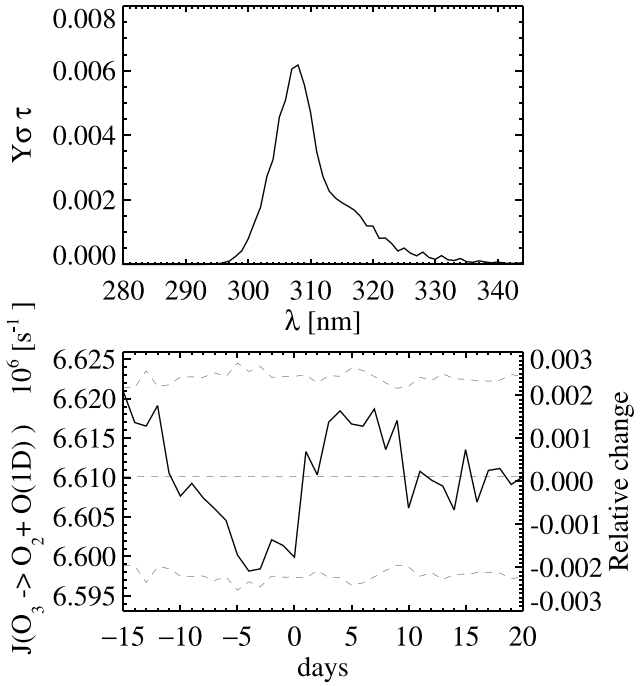

Figure 13. (top) The wavelength range where the reaction $O_3 + \gamma \rightarrow O_2 + O(1D)$ can occur in the lowest part of the atmosphere. The relatively narrow shape is a result of the atmospheric transmission $\tau(\lambda)$ cutoff at shorter wavelengths and the cross-section $\sigma(\lambda)$ cutoff at longer wavelengths. (bottom) Composite change in the photolysis constant for the reaction in equation (33), for the three largest FDs in the interval 2003–2006. Although there is a decrease in J, the change is only of the order $2-3 \times 10^{-3}$. The dashed lines are the 1σ variance.

Figure 13 (top) demonstrates that the range of wavelengths where the photoreaction occurs in the lower part of the atmosphere is quite narrow. Using observational data of the solar spectrum from either composite solar spectral irradiance covering the time period 8 November 1978 to 1 August 2005 [*DeLand and Cebula*, 2008] in the wavelength range 120–400 nm or the Solar Radiation and Climate Experiment (SORCE) covering the temporal period 14 April 2003 to 24 August 2015 (http://lasp.colorado.edu/home/sorce/data/), it is possible to study the changes in the above photochemical reaction during FDs. The results all show that the variations are of the order of a few parts per thousand. Namely, they are too small to be important. As an example, Figure 13 (bottom) depicts the variation in $J(O_3 + \gamma \rightarrow O_2 + O(1D), t)$ for the three strongest FDs since 2003. Notice that the relative variation is small, in particular, when compared to the typical variance shown as the dashed lines.

Moreover, the decrease in UV seen in Figure 13 (bottom) is not seen at wavelengths shorter than approximately $\lambda = 280$ nm, but an increase. Figure 14 displays the superposed change in UV at the wavelength $\lambda = 250$ nm centered on the three strongest FDs after 2003. Wavelengths shorter than $\lambda = 280$ nm do not penetrate into the troposphere, but UV with a wavelength $\lambda = 250$ nm has the largest absorption by ozone in the stratosphere. These shorter wavelengths are therefore important at the stratosphere.

A clear maximum in UV is seen at days 1 and 2, minima at days −5 and 14, respectively. The origin of these changes in UV are caused by the approximately 27 day solar rotation of active regions on the Sun. That this is the case can be seen from Figure 15, which depicts the change in UV at the wavelength $\lambda = 240.92$ nm over the 400 day period, 14 April 2003 to 15 October 2015. Here the changes in UV seem to follow the approximately 26 day solar rotation of active regions on the Sun. Since the FDs have their origin from coronal mass ejections from active regions, the intensity of the UV at this wavelength is close to maximum as the active region passes the solar disk, as is exemplified by the strongest FD in Oct. 2003 (marked with the red diamond symbol). This FD did not impact the UV in any notable way, which can be seen from the subsequent three solar rotations where a maxima in UV are seen but without any FD superimposed.

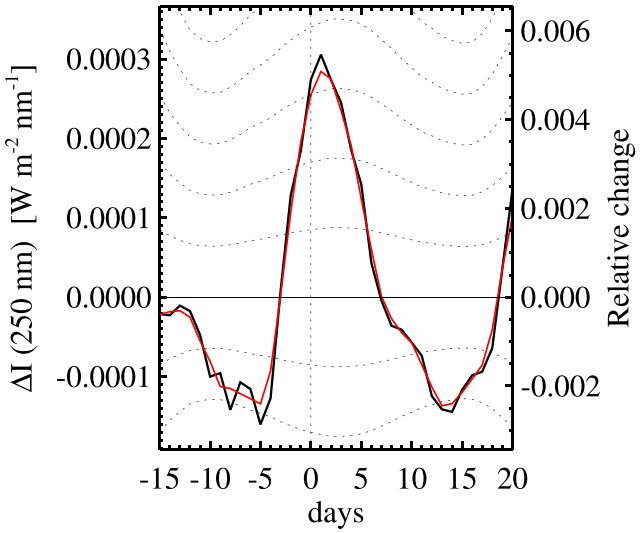

Figure 14. UV variation at $\lambda = 250$ nm superposed and centered at the three strongest FD after 2003 (data from FD 2 and FD 5 from Table 1 are not available in the SORCE data set). Notice that the relative change is of the order 0.8%. The maximum seen in UV is due to the rotation of active regions with a period of 27 days (see also Figure 15). Typically, an active region at maximum UV and a FD are closely correlated since a coronal mass ejection has to hit the Earth to generate a significant FD. The dashed lines are the $n\sigma$ variance, $n = 1, 2 \ldots$.

The question is now if such 26–27 day variations of typically 1 to 2% in UV in the stratosphere has an effect on clouds in the troposphere. In Figure 15 a number of 27 days UV variations are seen with variations equal to or larger than the 31 October 2003 event, whose maxima are marked with blue star symbols. The dates are 26 April 2003, 26 May 2003, 27 November 2003, 23 December 2003, and 21 January 2004. To answer the aforementioned question, Figure 16 displays the cloud fraction using "ISCCP all UV detected" data, where five time series are superposed over 36 days with day 0 being the date of maximum UV (shown as with the blue symbols in Figure 15). As can be seen from Figure 16, no statistical significant response is found (ASL = 83 %). It should be mentioned that since FDs are related to active regions, there is also a correlation between these active regions and cosmic ray variations. However, the dates used above for the UV maxima are not associated with any significant or strong FDs.

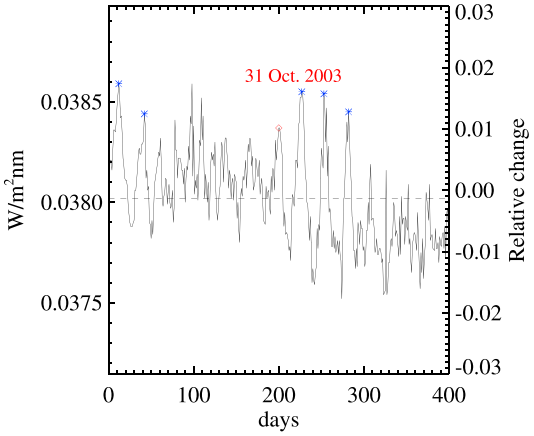

Figure 15. UV variation at $\lambda = 245$ nm as a function of time after 14 April 2003. The strongest FD event in October 2003 is marked with a red diamond symbol. Notice that the typical variation in UV is about 26–27 days and that the strong FD is not seen in the UV data. The blue symbols are maxima of 27 days rotation periods without any recording of a strong FD. The dates marked with the blue stars are 26 April 2003, 26 May 2003, 27 November 2003, 23 December 2003, and 21 January 2004.

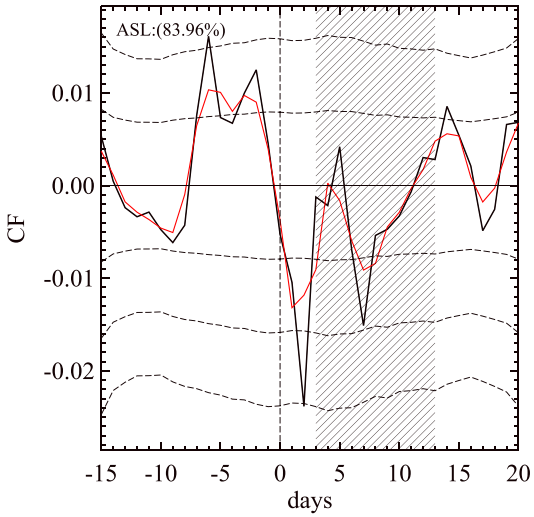

Figure 16. Cloud fraction from the ISCCP all UV data superposed over the five dates shown in Figure 15 with maximum UV. The dashed lines denote the $n - \sigma$ variance, with integer n.

Summarizing the above, the data suggests the following:

1. The relative changes in tropospheric photochemical reaction rates simultaneous with strong FDs are of the order of parts per thousand. This should be compared with the typical simultaneous changes in clouds of ≈3%. A cause and effect from photochemistry is unlikely since it would imply an amplification factor of ≈30.
2. UV wavelengths relevant to the stratosphere do show changes of the order 1–2% simultaneously with the strong FDs; however, similar changes in UV but on dates without strong FDs do not result in any significant cloud response. UV in the stratosphere is therefore unlikely to be the cause of the observed cloud changes during strong FDs.

7.2.2. Total Solar Irradiance

Total solar irradiance (TSI) exhibits a decrease with a minimum occurring approximately 2 days before the FD minimum, as seen in Figure 17 for five strongest FDs. The observed decrease is of the order 1 W/m^2, corresponding to a relative change of the order 0.0007 — a relative change similar to the change in the photolysis constant. Such a change, which after distributing the energy over the Earth and taking the Earth's albedo into account, is of the order 0.2 W/m^2, which is too small to make any significant impact on the atmosphere through any thermodynamic effects. It has been suggested that changes in the solar spectrum (mainly in the UV) can cause a warmer stratosphere that subsequently couples down to the troposphere over the 11 year solar cycle. But in the case of 0.2 W/m^2 over a few days, due to the large heat capacity in the Earth's system, the change is so minute that any thermodynamic response is negligible. Second, a priori there is no

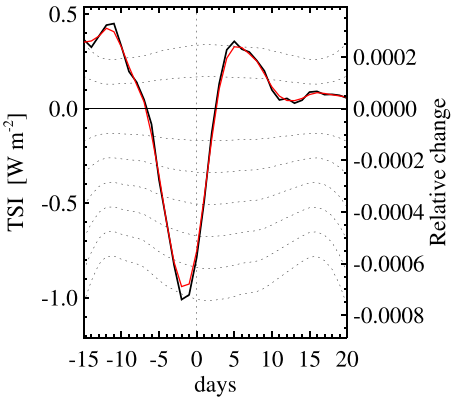

Figure 17. Variation of Total Solar Irradiance (TSI) around the mean for the five strongest FDs after 1998. The mean is 1365.6 W/m2 and the relative change is 0.001. The dashed lines denote the $n - \sigma$ variance, with integer n.

Table 5. List of the Six FDs Used in the Study of *Calogovic et al.* [2010] and Their Corresponding Ranking According to the List in This Study[a]

Calogovic Et Al.	Rank Order by Strength According to Table 1
1	13
2	8
3	5
4	10
5	24
6	15

[a]Notice that all rank low except FD 3 which ranks fifth on the present list.

mechanism that should relate the TSI with the observed changes in various CCN characteristics, such as their radius, since it depends on aerosol formation processes prior to the formation of clouds. Finally, similar to the argument used in the case of the photolysis constant, the relative variation in TSI is of the order 0.0007 and the corresponding changes in clouds are 0.03, which would imply an amplification factor of about 40 of the effect of TSI on clouds. This is unlikely.

7.3. The Global Electric Circuit

An alternative theory about how Forbush decreases may affect the atmosphere involves the downward ionosphere-Earth current density J_z that is a part of the global electric circuit. For example, *Tinsley and Deen* [1991] reported impacts of FDs on winter storm vorticity. Another example is *Kniveton et al.* [2008], who examined changes in fair-weather measurements of vertical electrical field at Vostok, Antarctica, and noted changes in ISCCP cloud data both at high latitudes and in the tropics. Although measurements of J_z and the electric potential are highly dependent on regional and meteorological conditions, it is suggested from modeling that there is a systematic zonal change in J_z following FDs and that such changes can influence cloud microphysics [*Tinsley et al.*, 2007]. These processes may then influence aerosol concentrations several days later. J_z has also been suggested to affect ice formation [*Tinsley et al.*, 2007]. In the present work we do not see any effect in ice clouds but cannot rule out a J_z effect in the liquid phase.

7.4. Comparison With Previous Studies

We can now use the results in this study to explore why some previous studies did not find significant responses to FDs. *Calogovic et al.* [2010] examined six FDs from the ISCCP IR low clouds data set and concluded that there is no effect to be found. Based on the present study, we note the following likely reasons as to why this conclusion was reached: First, ISCCP IR low clouds have a fairly weak signal in contrast to ISCCP all IR clouds as can be seen by comparing Figure 7 (bottom right) with Figure 7 (top right) or the signal-to-noise values of Table 4. As discussed previously, this is likely due to the satellite view of low clouds being obscured by clouds at higher levels. Second, the selected FDs in *Calogovic et al.* [2010] all rank low in our list. Table 5 compares the FDs used by *Calogovic et al.* [2010] with the ranking in Table 1. These choices make it difficult to observe a signal. Using the same six FDs and data from SSM/I, which has the highest signal-to-noise ratio, and applying the procedure in section 4, we find a result with a marginal 95.7% significance.

Kristjánsson et al. [2008] used MODIS data to examine the means of 22 FDs. For comparison, only 13 FDs in the same period of 2000–2006 were used in the present study, and most of the 22 FDs resulted in minor changes in ionization, with the result that the mean signal was obscured by the meteorological noise. This can be the reason *Kristjánsson et al.* [2008] found that there was no signal. When they looked at the six strongest events on their list (these events are also high on the ranking list in this study) their signal improved. *Sloan and Wolfendale* [2008] used ISCCP data but focused in part on monthly averaged data. As shown in the present study (section 7.1) and in *Svensmark et al.* [2009], the extremum of the effect occurs about a week after the FD minimum and last only a few days; monthly averages are unlikely to show a signal as the signal will be obscured by noise.

Laken et al. [2009] looked at MODIS data and considered a longer time series than 20 days ($\pm$40 days). They state that the maximum time for an aerosol particle to grow to CCN size is 2 days and conclude that a delay of about 5 days cannot be justified by any known process. However, a growth time of 5–7 days is in agreement

with observations, as discussed in section 7.1. Moreover, they assess that the fluctuations observed during FDs are more likely noise than a signal related to cosmic rays. However, they did not carry out a statistical study; e.g., there are no error bars/confidence intervals on their figures.

The study by *Svensmark et al.* [2009] was criticized for estimating the significance of FD signals based on an average variance over a 36 day interval, instead of a Monte Carlo estimate. This problem is avoided by the present approach.

8. Conclusion

By ranking the strength of Forbush decreases according to their expected impact on the ionization of the lower atmosphere, a FD strength-dependent response could be investigated.

A Monte Carlo bootstrap statistical procedure was defined which either considered the time series or the integrated response over the days following the FD minimum and was based on the expected growth time of aerosols. These statistical tests allowed for a calculation of an achieved significance level and so could provide information on the likelihood that there was a response in atmospheric aerosol and cloud parameters following FDs.

Four independent atmospheric data sets were used: (1) AERONET data using the Angstrom exponent in the wavelength range 330–440 nm. This parameter is related to the fine aerosol fraction. (2) SSM/I data measuring the cloud liquid water content over the oceans, (3) ISCCP data using IR detection of low, middle, high, and total cloud fraction, and finally, (4) MODIS data which allowed the study of a number of cloud microphysical parameters simultaneously. The parameters were cloud effective emissivity, cloud optical thickness, liquid water cloud fraction, column density of the cloud condensation nuclei, liquid water path, and finally, liquid cloud effective radius.

Responses (>95%) to FDs are found in almost all parameters of the analyzed data sets: AERONET: Angstrom exponent, a measure of aerosols and cloud condensation nuclei [CCN] changes; SSM/I: liquid water content; ISCCP: total, high, and middle IR clouds above oceans; MODIS: cloud effective emissivity, cloud optical thickness, liquid water, cloud fraction, liquid water path, liquid cloud effective radius. ISCCP low IR clouds above oceans are only significant at a 93% level. In this connection it was observed that MODIS liquid cloud fraction also has a clear response in contrast to MODIS ice cloud fraction, which indicates that the effect is mainly in liquid clouds. Since the total UV-detected clouds by ISCCP show a strong response, it suggests that this parameter is mainly influenced by liquid clouds. In contrast, variations in ISCCP low UV-detected clouds are influenced by overlap of clouds at other heights, since the satellites have only seen the top layer of clouds and is the likely reason for the small significance of this parameter. One MODIS parameter, column density of the cloud condensation nuclei, is found to be insignificant which is expected based on its high noise level; however, independent data from AERONET do show a response.

A positive, nonzero relation between the strength of the FDs and the size of the responses is found in all data sets.

Changes in UV or in TSI were found to be unlikely to explain the observed responses in clouds or aerosols following FDs, since that would require an amplification factor of 30–40.

We therefore conclude the following:

1. Responses are found in the cloud microphysical parameters in the days following Forbush decreases. The sign and size of the response in all the parameters are consistent with changes derived from cloud microphysics. The size of the responses are of the order of a 2% change in cloud fraction for the strongest FDs.
2. A correlation between the magnitude of the FD events and the effect on aerosol/cloud physics has been found in all data sets (AERONET, ISCCP, MODIS, and SSM/I).
3. The signs of the responses are as expected from a cosmic ray effect on cloud microphysics.

These results show with high confidence that there is a real impact of Forbush decreases on cloud microphysics. The suggested causal chain of reactions responsible for the observed correlations begins with a solar coronal mass ejection resulting in a FD with fewer cosmic rays → less atmospheric ionization → less aerosol nucleation → fewer formed CCN → fewer cloud droplets → larger cloud droplets, decrease in cloud fraction,

cloud optical thickness, and in cloud emissivity. Finally, since the droplets are larger, removal by rain is more likely and is consistent with the reduction in liquid water content. We note that a J_z mechanism cannot be ruled out.

In conclusion, the results support the suggestion that ions play a significant role in the life cycle of clouds.

Acknowledgments
We are grateful to the late Nigel Calder for helpful comments in the early stages of this work. We thank Torsten Bondo for his initial work on part of the programs used in the data analysis. We thank professor of statistics Henrik Spliid for valuable discussions regarding the statistics. We thank the two reviewers for their thorough and constructive reviews which have helped improve the paper. We acknowledge receipt of the unpublished TSI data from the VIRGO Experiment on the cooperative ESA/NASA Mission SOHO (version d41_61_0803) from PMOD/WRC, Davos, Switzerland. We are also grateful to the Cosmic Ray Section, Solar-Terrestrial Environment Laboratory, and Nagoya University who provided the muon data. Data can be obtained from http://www.stelab.nagoya-u.ac.jp/ste-www1/div3/muon/muon1.html We thank Tom Woods (CU LASP), Gary Rottman (CU LASP), and Giuliana de Toma (NCAR, HAO) for the SOLSTICE data and Mark Weber (U. Bremen, Germany) for the GOME data. MODIS data were obtained from http://modis.gsfc.nasa.gov. SSM/I data are produced by Remote Sensing Systems and sponsored by the NASA Earth Science REASoN DISCOVER Project. Data are available at http://www.remss.com. We thank the principal investigators and staff of AERONET (http://aeronet.gsfc.nasa.gov) for establishing and maintaining the sites used in this investigation. Martin B. Enghoff thanks the Carlsberg Foundation and the Danish Council for Independent Research/Natural Sciences for financial support.

References

Ahluwalia, H. S., and M. M. Fikani (2007), Cosmic ray detector response to transient solar modulation: Forbush decreases, *J. Geophys. Res.*, *112*, A08105, doi:10.1029/2006JA011958.

Bagó, E. P., and C. J. Butler (2000), The influence of cosmic rays on terrestrial clouds and global warming, *Astron. Geophys.*, *41*(4), 4.18–4.22.

Bazilevskaya, G. A., et al. (2008), Cosmic ray induced ion production in the atmosphere, *Space Sci. Rev.*, *137*, 149–173, doi:10.1007/s11214-008-9339-y.

Bondo, T., M. B. Enghoff, and H. Svensmark (2010), Model of optical response of marine aerosols to Forbush decreases, *Atmos. Chem. Phys.*, *10*, 2765–2776.

Boucher, O., et al. (2013), Clouds and aerosols, in *Climate Change 2013: The Physical Science Basis. Contribution of Working Group I to the Fifth Assessment Report of the Intergovernmental Panel on Climate Change*, edited by T. F. Stocker et al., Cambridge Univ. Press, Cambridge, U. K., and New York.

Brest, C. L., W. B. Rossow, and M. D. Roiter (1997), Update of radiance calibrations for ISCCP, *J. Atmos. Oceanic Technol.*, *14*, 1091–1109, doi:10.1175/1520-0426(1997)014<1091:UORCFI>2.0.CO;2.

Calogovic, J., C. Albert, F. Arnold, J. Beer, L. Desorgher, and E. O. Flueckiger (2010), Sudden cosmic ray decreases: No change of global cloud cover, *Geophys. Res. Lett.*, *37*, L03802, doi:10.1029/2009GL041327.

Clem, J. M., and L. I. Dorman (2000), Neutron monitor response functions, *Space Sci. Rev.*, *93*, 335–359, doi:10.1023/A:1026508915269.

DeLand, M. T., and R. P. Cebula (2008), Creation of a composite solar ultraviolet irradiance data set, *J. Geophys. Res.*, *113*(A11), A11103, doi:10.1029/2008JA013401.

Dickinson, R. E. (1975), Solar variability and the lower atmosphere, *Bull. Am. Meteorol. Soc.*, *56*(12), 1240–1248.

Dragić, A., I. Aničin, R. Banjanac, V. Udovičić, D. Joković, D. Maletić, and J. Puzović (2011), Forbush decreases—Clouds relation in the neutron monitor era, *Astrophys. Space Sci. Trans.*, *7*, 315–318, doi:10.5194/astra-7-315-2011.

Efron, B., and R. J. Tibshirani (1994), *An Introduction to the Bootstrap*, Chapman & Hall/CRC Monographs on Statistics & Applied Probability, CRC Press, New York.

Flückiger, E. O., M. R. Moser, B. Pirard, R. Bütikofer, and L. Desorgher (2008), A parameterized neutron monitor yield function for space weather applications, in *Proceedings of the 30th International Cosmic Ray Conference*, vol. 1, pp. 289–1109.

Forbush, S. (1937), A model for particle formation and growth in the atmosphere with molecular resolution in size, *Phys. Rev.*, *51*, 1108.

Harrison, R., and D. B. Stephenson (2006), Empirical evidence for a nonlinear effect of galactic cosmic rays on clouds, *Proc. R. Soc. London, Ser. A*, *462*(2068), 1221–1233, doi:10.1098/rspa.2005.1628.

Harrison, R. G., and M. H. Ambaum (2010), Observing Forbush decreases in cloud at Shetland, *J. Atmos. Sol. Terr. Phys.*, *72*(18), 1408–1414, doi:10.1016/j.jastp.2010.09.025.

Heck, D., J. Knapp, J. N. Capdevielle, G. Schatz, and T. Thouw (1998), *CORSIKA: A Monte Carlo Code to Simulate Extensive Air Showers*, Wissenchaftliche Berichte, Forschungszentrum, Karlsruhe FZKA 6019, Hannover, Germany.

Hobbs, P. V. (1993), *Aerosol-Cloud-Climate Interactions*, Academic Press, San Diego, Calif.

Howard, D., N. J. Shaviv, and H. Svensmark (2015), The solar and southern oscillation components in the satellite altimetry data, *J. Geophys. Res. Space Physics*, *120*(5), 3297–3306, doi:10.1002/2014JA020732.

Kazil, J., E. R. Lovejoy, M. C. Barth, and K. O'Brien (2006), Aerosol nucleation over oceans and the role of galactic cosmic rays, *Atmos. Chem. Phys.*, *6*, 4905–4924.

King, M. D., S.-C. Tsay, S. E. Platnick, M. Wang, and K.-N. Liou (1997), Cloud retrieval algorithms for MODIS: Optical thickness, effective particle radius, and thermodynamic phase, Tech. Rep. MODIS Algorithm Theoretical Basis Document No. ATBD-MOD-05.

Kirkby, J., et al. (2011), Role of sulphuric acid, ammonia and galactic cosmic rays in atmospheric aerosol nucleation, *Nature*, *476*, 429–433, doi:10.1038/nature10343.

Kniveton, D., B. Tinsley, G. Burns, E. Bering, and O. Troshichev (2008), Variations in global cloud cover and the fair-weather vertical electric field, *J. Atmos. Sol. Terr. Phys.*, *70*(13), 1633–1642, doi:10.1016/j.jastp.2008.07.001.

Kristjánsson, J. E., C. W. Stjern, F. Stordal, A. M. Fjæraa, G. Myhre, and K. Jónasson (2008), Cosmic rays, cloud condensation nuclei and clouds—A reassessment using MODIS data, *Atmos. Chem. Phys.*, *8*, 7373–7387.

Kulmala, M., H. Vehkamäki, T. Petäjä, M. Dal Maso, A. Lauri, V. M. Kerminin, W. Birmili, and P. H. McMurry (2004), Formation and growth rates of ultrafine atmospheric particles: A review of observations, *J. Aerosol Sci.*, *35*, 143–176.

Laken, B., A. Wolfendale, and D. Kniveton (2009), Cosmic ray decreases and changes in the liquid water cloud fraction over the oceans, *Geophys. Res. Lett.*, *36*, L23803, doi:10.1029/2009GL040961.

Laken, B., D. Kniveton, and A. Wolfendale (2011), Forbush decreases, solar irradiance variations, and anomalous cloud changes, *J. Geophys. Res.*, *116*, D09201, doi:10.1029/2010JD014900.

Laken, B. A., and J. Calogovic (2011), Solar irradiance, cosmic rays and cloudiness over daily timescales, *Geophys. Res. Lett.*, *38*(24), L24811, doi:10.1029/2011GL049764.

Levy, R. C., L. A. Remer, R. G. Kleidman, S. Mattoo, C. Ichoku, R. Kahn, and T. F. Eck (2010), Global evaluation of the collection 5 MODIS dark-target aerosol products over land, *Atmos. Chem. Phys.*, *10*(21), 10,399–10,420.

Marsh, N. D., and H. Svensmark (2000), Low cloud properties influenced by cosmic rays, *Phys. Rev. Lett.*, *85*, 5004–5007, doi:10.1103/PhysRevLett.85.5004.

Miller, J. N., and J. C. Miller (2000), *Statistics and Chemometrics for Analytical Chemistry*, 4th ed., Prentice Hall, Englewood Cliffs, N. J.

Pierce, J. R., and P. J. Adams (2009), Can cosmic rays affect cloud condensation nuclei by altering new particle formation rates?, *Geophys. Res. Lett.*, *36*, L09820, doi:10.1029/2009GL037946.

Platnick, S., M. King, S. Ackerman, W. Menzel, B. Baum, J. Riedi, and R. Frey (2003), The MODIS cloud products: Algorithms and examples from Terra, *IEEE Trans. Geosci. Remote Sens.*, *41*(2), 459–473.

Pudovkin, M. I., and S. V. Veretenenko (1995), Cloudiness decreases associated with Forbush decreases of galactic cosmic rays, *J. Atmos. Sol. Terr. Phys.*, *57*, 1349–1355.

Remer, L., et al. (2005), The MODIS aerosol algorithm, products, and validation, *J. Atmos. Sci.*, *62*(4), 947–973, doi:10.1175/JAS3385.1.

Rohs, S., R. Spang, F. Rohrer, C. Schiller, and H. Vos (2010), A correlation study of high-altitude and midaltitude clouds and galactic cosmic rays by MIPAS-Envisat, *J. Geophys. Res.*, *115*, D14212, doi:10.1029/2009JD012608.

Rossow, W. B., and R. A. Schiffer (1991), ISCCP cloud data products, *Bull. Am. Meteorol. Soc.*, *72*, 2–20, doi:10.1175/1520-0477(1991)072<0002:ICDP>2.0.CO;2.

Salomonson, V. V., W. L. Barnes, P. W. Maymon, H. E. Montgomery, and H. Ostrow (1989), MODIS—Advanced facility instrument for studies of the Earth as a system, *IEEE Trans. Geosci. Remote Sens.*, *27*, 145–153, doi:10.1109/36.20292.

Sanuki, T., et al. (2000), Precise measurement of cosmic-ray proton and helium spectra with the BESS spectrometer, *Astro. Phys. J.*, *545*, 1135–1142, doi:10.1086/317873.

Schuster, G. L., O. Dubovik, and B. N. Holben (2006), Angstrom exponent and bimodal aerosol size distributions, *J. Geophys. Res.*, *111*, D07207, doi:10.1029/2005JD006328.

Shaviv, N. J. (2008), Using the oceans as a calorimeter to quantify the solar radiative forcing, *J. Geophys. Res.*, *113*(A12), A11101, doi:10.1029/2007JA012989.

Sloan, T., and A. W. Wolfendale (2008), Testing the proposed causal link between cosmic rays and cloud cover, *Environ. Res. Lett.*, *3*(4), 024001, doi:10.1088/1748-9326/3/2/024001.

Snow-Kropla, E., J. Pierce, D. Westervelt, and W. Trivitayanurak (2011), Cosmic rays, aerosol formation and cloud-condensation nuclei: Sensitivities to model uncertainties, *Atmos. Chem. Phys.*, *11*, 4001–4013.

Stephens, G. L. (1978), Radiation profiles in extended water clouds. II: Parameterization schemes, *J. Atmos. Sci.*, *35*, 2123–2132.

Svensmark, H., and E. Friis-Christensen (1997), Variation of cosmic ray flux and global cloud coverage—A missing link in solar-climate relationships, *J. Atmos. Sol. Terr. Phys.*, *59*, 1225–1232, doi:10.1016/S1364-6826(97)00001-1.

Svensmark, H., J. O. P. Pedersen, N. D. Marsh, M. B. Enghoff, and U. I. Uggerhøj (2007), Experimental evidence for the role of ions in particle nucleation under atmospheric conditions, *Proc. R. Soc. London, Ser. A*, *463*(2078), 385–396.

Svensmark, H., T. Bondo, and J. Svensmark (2009), Cosmic ray decreases affect atmospheric aerosols and clouds, *Geophys. Res. Lett.*, *36*, L15101, doi:10.1029/2009GL038429.

Svensmark, H., M. B. Enghoff, and J. O. P. Pedersen (2013), Response of cloud condensation nuclei (>50 nm) to changes in ion-nucleation, *Phys. Lett. A*, *377*, 2343–2347, doi:10.1016/j.physleta.2013.07.004.

Tinsley, B. A., and G. W. Deen (1991), Apparent tropospheric response to MeV-GeV particle flux variations: A connection via electrofreezing of supercooled water in high-level clouds?, *J. Geophys. Res.*, *96*(D12), 22,283–22,296, doi:10.1029/91JD02473.

Tinsley, B. A., G. Burns, and L. Zhou (2007), The role of the global electric circuit in solar and internal forcing of clouds and climate, *Adv. Space Res.*, *40*(7), 1126–1139, doi:10.1016/j.asr.2007.01.071.

Todd, M. C., and D. R. Kniveton (2004), Short-term variability in satellite-derived cloud cover and galactic cosmic rays: An update, *J. Atmos. Terr. Phys.*, *66*, 1205–1211.

Usoskin, I. G., and G. A. Kovaltsov (2006), Cosmic ray induced ionization in the atmosphere: Full modelling and practical applications, *J. Geophys. Res.*, *111*, D21206, doi:10.1029/2006JD007150.

Weng, F., N. C. Grody, R. R. Ferraro, Q. Zhao, and C. T. Chen (1997), Global cloud water distribution derived from special sensor microwave imager/sounder and its comparison with GCM simulation, *Adv. Space Res.*, *19*, 407–411, doi:10.1016/S0273-1177(97)00048-3.

Wentz, F. J. (1997), A well-calibrated ocean algorithm for special sensor microwave/imager, *J. Geophys. Res.*, *102*, 8703–8718, doi:10.1029/96JC01751.

Woods, T., F. Eparvier, J. Fontenla, J. Harder, G. Kopp, W. McClintock, G. Rottman, B. Smiley, and M. Snow (2004), Solar irradiance variability during the October 2003 solar storm period, *Geophys. Res. Lett.*, *31*, L10802, doi:10.1029/2004GL019571.

Yu, F., and G. Luo (2014), Effect of solar variations on particle formation and cloud condensation nuclei, *Environ. Res. Lett.*, *9*(4), 045004.